

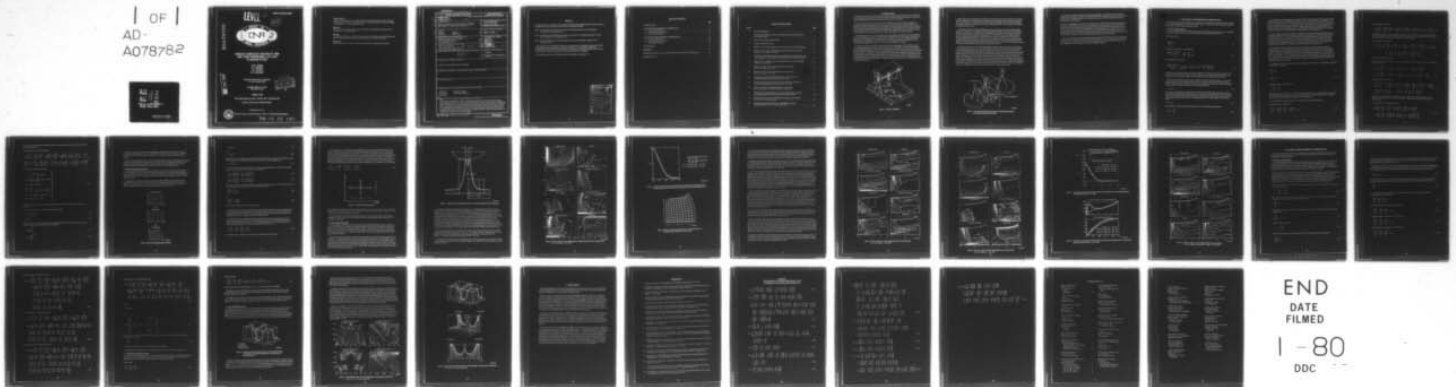
AD-A078 782

MCDONNELL DOUGLAS RESEARCH LABS ST LOUIS MO
VISCIOUS FLOWFIELDS INDUCED BY TWO- AND THREE-DIMENSIONAL LIFT J--ETC(U)
MAR 79 W W BOWER , R K AGARWAL , G R PETERS N00014-76-C-0494
ONR-CR215-246-3F NL

F/G 20/4

UNCLASSIFIED

1 OF 1
AD-A078782



END
DATE
FILMED
1-80
DDC

LEVEL

REPORT ONR-CR215-246-3F

ADA 078782

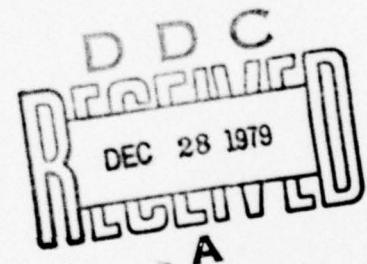


**VISCOUS FLOWFIELDS INDUCED BY TWO-
AND THREE-DIMENSIONAL LIFT JETS
IN GROUND EFFECT**

**W.W. BOWER
R.K. AGARWAL
G.R. PETERS
D.R. KOTANSKY**

**McDonnell Douglas Research Laboratories
St. Louis, Missouri 63166**

**CONTRACT N00014-76-C-0494
ONR TASK 215-246**



DDC FILE COPY

1 March 1979

Final Technical Report for Period 1 February 1976 - 28 February 1979

Approved for public release distribution unlimited.



PREPARED FOR THE

OFFICE OF NAVAL RESEARCH • 800 N. QUINCY ST. • ARLINGTON • VA • 22217

79-12 27 102

Change of Address

Organizations receiving reports on the initial distribution list should confirm correct address. This list is located at the end of the report. Any change of address or distribution should be conveyed to the Office of Naval Research, Code 211, Arlington, VA 22217.

Disposition

When this report is no longer needed, it may be transmitted to other organizations. Do not return it to the originator or the monitoring office.

Disclaimer

The findings and conclusions contained in this report are not to be construed as an official Department of Defense or Military Department position unless so designated by other official documents.

Reproduction

Reproduction in whole or in part is permitted for any purpose of the United States Government.

UNCLASSIFIED

SECURITY CLASSIFICATION OF THIS PAGE (When Data Entered)

19 REPORT DOCUMENTATION PAGE		READ INSTRUCTIONS BEFORE COMPLETING FORM
1. REPORT NUMBER ONR CR215-246-3F	2. GOVT ACCESSION NO.	3. RECIPIENT'S CATALOG NUMBER
4. TITLE (and Subtitle) VISCIOUS FLOWFIELDS INDUCED BY TWO- AND THREE- DIMENSIONAL LIFT JETS IN GROUND EFFECT.		5. TYPE OF REPORT & PERIOD COVERED Final Technical Report 1 Feb 76 - 28 Feb 79
7. AUTHOR(s) W.W. Bower, G.R. Peters R.K. Agarwal, D.R. Kotansky		6. PERFORMING ORG. REPORT NUMBER
9. PERFORMING ORGANIZATION NAME AND ADDRESS McDonnell Douglas Research Laboratories McDonnell Douglas Corporation St. Louis, Missouri 63166		8. CONTRACT OR GRANT NUMBER(s) N00014-76-C-0494
11. CONTROLLING OFFICE NAME AND ADDRESS Office of Naval Research Vehicle Technology Program, Code 211 800 N. Quincy Street, Arlington, VA 22217		10. PROGRAM ELEMENT, PROJECT, TASK AREA & WORK UNIT NUMBERS 61153N-14 RR014-11-84 NR215-246
14. MONITORING AGENCY NAME & ADDRESS (if different from Controlling Office) 12 38		12. REPORT DATE 1 Mar 79
		13. NUMBER OF PAGES
		15. SECURITY CLASS. (of this report) Unclassified
		15a. DECLASSIFICATION/DOWNGRADING SCHEDULE
16. DISTRIBUTION STATEMENT (of this Report) Approved for public release; distribution unlimited		
17. DISTRIBUTION STATEMENT (of the abstract entered in Block 20, if different from Report)		
18. SUPPLEMENTARY NOTES		
19. KEY WORDS (Continue on reverse side if necessary and identify by block number) VTOL lift jet Turbulence modeling Ground effect Finite-difference methods Viscous flow		
20. ABSTRACT (Continue on reverse side if necessary and identify by block number) An important consideration for VTOL aircraft design is the aerodynamic interaction between airframe undersurfaces and the ground. In an effort to predict this phenomenon, a second-order-accurate, finite-difference scheme for solution of the two- and three-dimensional conservation equations of fluid mechanics, in combination with a turbulence model, is described. The solution technique is applied to a planar lift jet in ground effect for both incompressible and compressible flow and to two interacting incompressible jets with fountain formation. Fluid properties that characterize the jet impingement flowfields are given for a range of Reynolds numbers, and comparisons with measured data are presented. ←		

DD FORM 1 JAN 73 1473

EDITION OF 1 NOV 65 IS OBSOLETE

405 315

UNCLASSIFIED

SECURITY CLASSIFICATION OF THIS PAGE (When Data Entered)

PREFACE

This final report is an account of the work completed at the McDonnell Douglas Research Laboratories on Office of Naval Research Contract No. N00014-76-C-0494 under the following three phases:

- Phase 1 Viscous Flowfields and Airframe Forces Induced by Two-Dimensional Lift Jets in Ground Effect
(1 February 1976 to 28 February 1977)
- Phase 2 Compressible Viscous Flowfields and Airframe Forces Induced by Two-Dimensional Lift Jets in Ground Effect (1 February 1977 to 28 February 1978)
- Phase 3 Viscous Flowfields Induced by Three-Dimensional Lift Jets in Ground Effect (1 February 1978 to 28 February 1979)

This work was done in the Flight Sciences Department, managed by Dr. R.J. Hakkinen. The principal investigator for the first phase was Dr. D.R. Kotansky; the principal investigator for the second and third phases was Dr. W.W. Bower. The flowfield numerical work was done by Dr. Bower, Dr. R.K. Agarwal, and Dr. G.R. Peters. The computer graphics routines were written by Mr. P.W. Bierdeman and Mr. G.P. Tomaschke.

The program monitor was Dr. R.E. Whitehead, Office of Naval Research, Arlington, VA.

Accession For	
NTIS GRA&I	<input checked="checked" type="checkbox"/>
DDC TAB	<input type="checkbox"/>
Unannounced	<input type="checkbox"/>
Justification	
By _____	
Distribution/	
Availability Codes	
Dist	Avail and/or special
A	

TABLE OF CONTENTS

	Page
1. INTRODUCTION	1
2. ANALYSIS OF TWO-DIMENSIONAL IMPINGING JETS	4
2.1 The Governing Equations	4
2.2 The Numerical Solution Scheme	8
2.3 The Computed Flowfields	10
3. ANALYSIS OF THREE-DIMENSIONAL IMPINGING JETS	19
3.1 The Governing Equations	19
3.2 The Numerical Solution Scheme	22
3.3 The Computed Flowfields	23
4. CONCLUSIONS	26
REFERENCES	27
APPENDIX: Definitions of Functions Appearing in the Governing Equations for Planar Flow	28
DISTRIBUTION LIST	31

LIST OF ILLUSTRATIONS

Figure		Page
1	The planar impinging jet	1
2	Two interacting, initially axisymmetric jets impinging perpendicularly on the ground with fountain formation.	2
3	Inverse conformal mapping with stretching	8
4	Five-point finite-difference stencil	10
5	Definition of the computational region for the free-upper-boundary planar impinging jet	11
6	Property contours for the incompressible free-upper-boundary planar jet in ground effect ($h = 1$, $w = 2.5$, $Re = 1.27 \times 10^5$)	12
7	Comparison of experimental and theoretical ground-plane pressure distributions for the normal impingement of the free-upper-boundary planar jet with a fully developed profile	13
8	Definition of the computational region in the physical plane for a simulated fuselage undersurface in ground effect	13
9	Property contours for the incompressible planar jet in ground effect ($H = 2$, $W = 3.68$, $Re = 1.00 \times 10^2$)	15
10	Property contours for the incompressible planar jet in ground effect ($H = 2$, $W = 3.68$, $Re = 1.30 \times 10^5$)	16
11	Comparison of experimental and theoretical pressure distributions for the incompressible planar jet in ground effect ($H = 2$, $W = 3.68$)	17
12	Comparison of experimental and theoretical centerline property distributions for the incompressible planar jet in ground effect ($H = 2$, $W = 3.68$)	17
13	Property contours for the compressible planar jet in ground effect ($H = 2$, $W = 3.68$, $Re = 1.00 \times 10^2$, $Pr = 0.68$, $Fr = 1.63 \times 10^2$)	18
14	Definition of the computational region for two interacting, initially axisymmetric jets impinging perpendicularly on the ground with fountain formation	23
15	Representative contours for the incompressible interacting jets in ground effect ($L = 3$, $h = 1$, $w = 1$, $Re = 1.00 \times 10^2$)	24
16	Representative particle pathlines for the incompressible interacting jets in ground effect ($L = 3$, $h = 1$, $w = 1$, $Re = 1.00 \times 10^2$)	25

I. INTRODUCTION

With the current interest in jet and fan-powered vertical-takeoff-and-landing (VTOL) military aircraft, there has been an increasing demand for improved performance-prediction methods. This demand is greatest for techniques to predict propulsion-induced aerodynamic effects in the hover mode of VTOL flight.

This task is not easy, however, since the hover mode of a VTOL aircraft is characterized by complex flow phenomena. Ambient air is entrained into the lift jets and the wall jets, leading to an induced downflow of air around the aircraft and a resulting suckdown force. In addition, the inward jet flows collide and create a stagnation region from which a hot gas fountain emerges and impinges on the lower fuselage surface. The fountain is a source of positive induced forces which, to some extent, counteract the large suckdown forces near the ground. However, the fountain also heats the airframe surface and can result in the reingestion of hot gas into the inlet.

The VTOL ground-effect flow is characterized by three-dimensionality, high turbulence levels, compressibility, strong pressure gradients, and regions of stagnation-point and separated flow. In order to gain a fundamental understanding of lift-jet induced flows, including entrainment and fountain characteristics, the McDonnell Douglas Research Laboratories (MDRL) has over the past three years conducted a theoretical investigation of two- and three-dimensional impinging jets, under contract to the Office of Naval Research (ONR).

In the first two years of the contract, attention was focused on a single, planar, unvectored lift jet in ground effect, illustrated schematically in Figure 1. The jet exits from a slot of width \bar{D} in a contoured upper-surface a distance \bar{H} above the ground plane. The region of interest extends a distance \bar{W} on each side of the jet centerline. The jet flowfield can be characterized by the following three regions: a free-jet region in which the flow is essentially the same as that of a jet issuing into an unbounded region of the same fluid; the impingement region in which the flow changes direction with a large pressure gradient; and the wall-jet region in which the flow traverses the surface with zero pressure gradient. The fluid surrounding the jet is entrained at its boundaries in all three regions. This entrainment results in an induced secondary $\bar{p} - \bar{w}$ which can produce suckdown forces on the airframe undersurface and an associated lift loss.

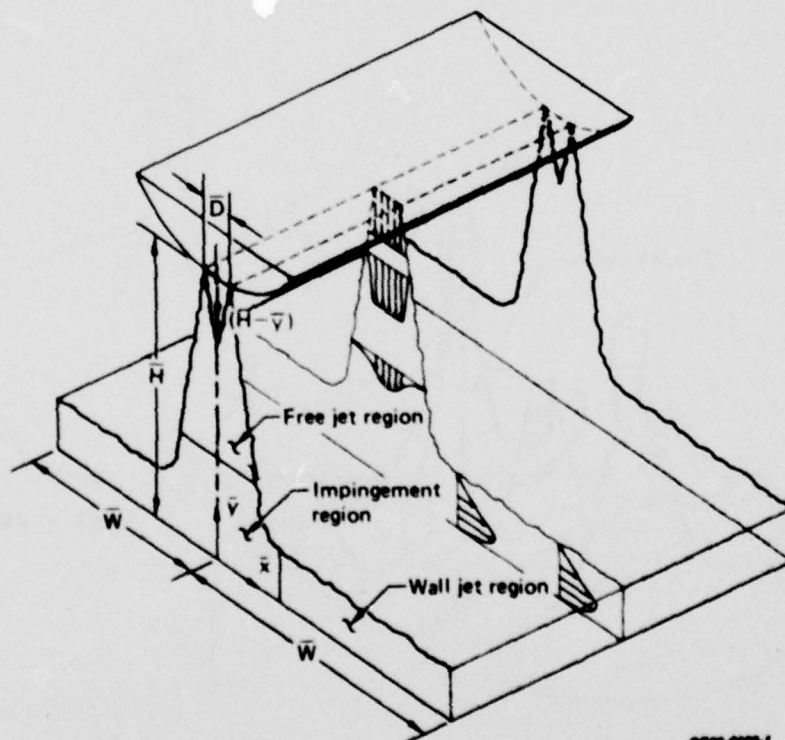


Figure 1. The planar impinging jet.

Isolated regions of the flowfield illustrated in Figure 1 can be analyzed with simplified techniques; for example, Rubel¹ has predicted the ground-plane pressure distributions in the impingement region using an incompressible, inviscid, rotational model for two-dimensional flow. Although good agreement has been obtained with measured ground-plane pressures, this approach cannot provide the fuselage undersurface pressure variation that is necessary to calculate the suckdown force.

A more rigorous analysis of the planar impinging jet, based on solution of the time-averaged Navier-Stokes equations in conjunction with a turbulence model, has been adopted by MDRL in its contract work with ONR. In the first year of this effort, an isolated, planar, incompressible lift jet in ground effect was analyzed, and in the second year this analysis was extended to compressible flow. In both endeavors, the time-averaged conservation equations, combined with an appropriate turbulence model, were solved in stream-function/vorticity form. A conformal mapping procedure was used to transform the nonrectangular physical plane into a rectangular computational plane, and a second-order-accurate, finite-difference scheme that is stable for all Reynolds numbers was applied to the transformed differential equations. The discretized system was solved iteratively using point relaxation for a range of the dimensionless parameters which characterize the problem.

In the third year of the contract work with ONR, MDRL extended its Navier-Stokes analysis of impinging jets to three-dimensional geometries. The configuration of primary interest, shown schematically in Figure 2, consists of two interacting, initially axisymmetric jets with fountain formation. The jets exit from two axisymmetric nozzles, each with diameter \bar{D} , whose centerlines are separated by a distance \bar{L} and whose exit planes are a distance \bar{H} above the ground. The width of the region of interest is the dimension \bar{W} , measured from the jet centerline. As in the case of the planar jet, the flowfield can be characterized by free-jet, impingement, and wall-jet regions. In addition, a fountain-upwash region is formed as a result of the interaction of the opposing wall jets. The inclination of the fountain is dependent on the geometry of the configuration and the ratio of the jet strengths. The fountain is a key element of the problem and the major motivation for analyzing this geometry, for as Walters and Henderson² conclude in an assessment of current methods to predict the aerodynamics of V/STOL aircraft, "a major deficiency exists both in available data base and prediction methods relative to fountain-induced effects."

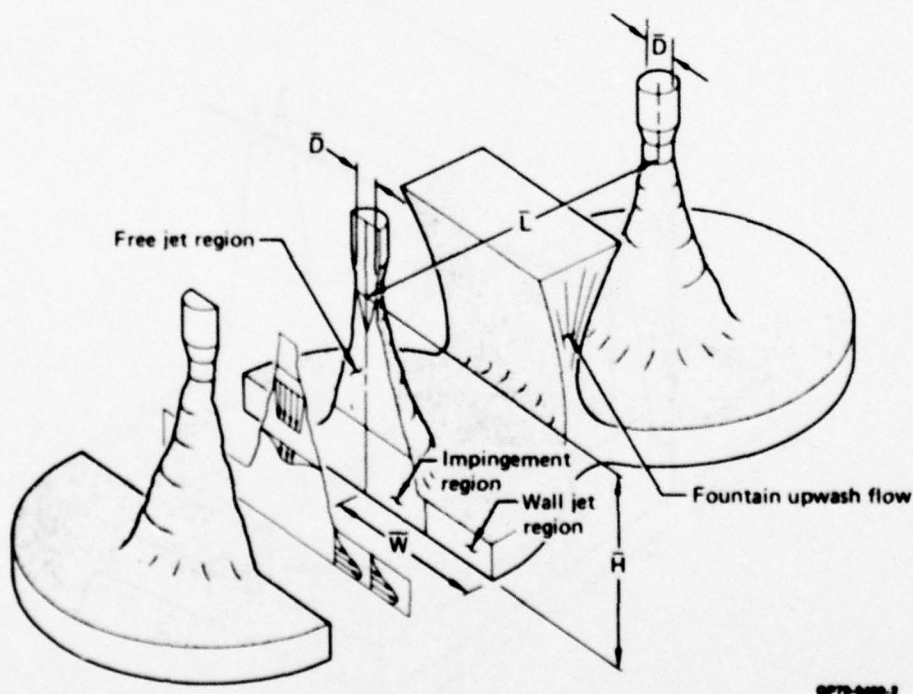


Figure 2. Two interacting, initially axisymmetric jets impinging perpendicularly on the ground with fountain formation.

An incompressible, inviscid, rotational flow model that is applicable to three-dimensional, jet-impingement problems has been described by Rubel³. This technique has been used to compute in a cartesian coordinate system an axisymmetric jet impinging perpendicular to the ground, but calculations of interacting jets with fountain formation have not been reported.

The basis of the MDRL approach adopted in the ONR contract for predicting three-dimensional, impinging jet flows is again a finite-difference solution of the time-averaged, Navier-Stokes equations with a complementary turbulence model. The conservation equations were solved in terms of scalar and vector potential functions and vorticity. Since the solution domain is a parallelepiped, a conformal mapping was not required. Solutions of the governing equations were obtained with an extension to three dimensions of the second-order-accurate, finite-difference algorithm used in the planar-jet analysis. An iterative solution of the discretized system of equations was obtained with line relaxation for selected dimensionless parameters which define the problem.

This report describes the theoretical approach that has been adopted in the ONR contract work to compute two- and three-dimensional impinging jets. The flowfield model, numerical solution scheme, and representative results which illustrate the computed entrainment and fountain-upwash characteristics are presented. The direction of future MDRL work in the calculation of ground-effect flowfields is discussed.

2. ANALYSIS OF TWO-DIMENSIONAL IMPINGING JETS

In this section, the procedure is described for computing the incompressible and compressible turbulent flowfields for the unvectored planar lift jet in ground effect shown in Figure 1. Contour plots of the calculated flow variables and comparisons with experimental data are presented.

2.1 The Governing Equations

The time-averaged continuity, momentum (Navier-Stokes), and thermal energy equations for steady compressible flow are given below in tensor notation for a space-fixed reference through which the fluid flows.

Conservation of mass:

$$\frac{\partial(\bar{\rho}\bar{u}_j)}{\partial x_j} = 0 \quad (1)$$

Conservation of momentum in the i th direction:

$$\frac{\partial(\bar{\rho}\bar{u}_i\bar{u}_j + \overline{\rho u_i'' u_j''})}{\partial x_j} = -\frac{\partial \bar{p}}{\partial x_i} + \frac{\partial \bar{\tau}_{ij}}{\partial x_j} + \bar{\rho} \bar{g}_i \quad (2)$$

Conservation of thermal energy:

$$\frac{\partial(\bar{\rho}\bar{u}_j \bar{J} + \overline{\rho u_j'' h''})}{\partial x_j} = \frac{\partial}{\partial x_j} \left[\bar{u}_i (\bar{\tau}_{ij} - \overline{\rho u_i'' u_j''}) + u_i'' (\bar{\tau}_{ij} - \frac{1}{2} \overline{\rho u_i'' u_j''}) \right] - \frac{\partial \bar{q}_j}{\partial x_j} \quad (3)$$

In these equations, ρ denotes density, u_i the velocity component in the i th direction, p the static pressure, τ_{ij} the shear stress in the i th direction on a surface normal to the j th direction, g_i the acceleration due to gravity in the i th direction, J the total specific enthalpy, h the static enthalpy, and q_j the heat flux in the j th direction.

Equations (1) through (3) are written in the form derived by Rubesin and Rose⁴ in which ρ , p , τ_{ij} , and q_j are represented using the usual Reynolds decomposition and u_i , J , and h are represented using the mass-averaged variables introduced by Favre⁵. Specifically, in the Reynolds decomposition, a general flow variable ϕ is expressed as the sum of a time-averaged component $\bar{\phi}$ and a fluctuating component ϕ' :

$$\phi = \bar{\phi} + \phi' \quad (4)$$

For the case of compressible flow, this approach is not the best for all variables because the resulting equations contain numerous explicit mean-product fluctuation terms arising from compressibility and do not have the same form as their incompressible counterparts. If, however, certain variables are written as mass-averaged variables, the resulting equations have virtually a term-by-term correspondence with the constant-property case. In the Favre system,

$$\phi = \tilde{\phi} + \phi'' \quad (5)$$

where the tilde, $\tilde{}$, denotes a mass average defined in terms of the conventional time average and

$$\phi'' = \phi' - \frac{\bar{\rho} \phi'}{\bar{\rho}} \quad (6)$$

The time-averaged conservation Equations (1) through (3) have the same form as the instantaneous conservation equations with the exception of the Reynolds stress term $-\rho u_i'' u_j''$, the Reynolds heat flux term $\rho u_j'' h''$, and the mean-energy dissipation term $u_i'' (\tau_{ij} - 1/2 \rho u_i'' u_j'')$. Moreover, these equations essentially have the desired term-by-term correspondence with the incompressible time-averaged conservation equations. This correspondence can be significant, as pointed out in Reference 4, if the basic turbulence mechanisms in the compressible flow remain similar to those in the constant-property flow (the so-called Morkovin hypothesis) such that turbulence modeling information can be taken from incompressible flow data and applied to the compressible case.

In order to obtain a closed system of equations, the Reynolds stress term, the Reynolds heat flux term, and the mean-energy dissipation term must be evaluated. In initial work on the planar jet, reported in References 6 and 7, one-equation models were used to represent the turbulence field (the Wolfshtein model⁸ for the incompressible jet and Rubesin's extension of the Glushko model⁹ for the compressible jet). Both of these approaches suffer because the turbulence length-scale distributions must be specified. For this reason, more recent analyses of the incompressible and compressible planar jets have used the two-equation Jones-Launder turbulence model¹⁰ in which the length-scale variations are implicit in the analysis and need not be specified *a priori*.

When Equations (1) and (3) are expanded from tensor notation into cartesian coordinates (x,y) with the corresponding velocity components (u,v), the result is the so-called primitive-variable form of the time-averaged conservation equations for a compressible planar flow. In the present work the equations are not solved, however, in terms of the primitive variables (velocity components and static pressure). The reason for this, as indicated by Ghia et al. in Reference 11, is that the pressure does not appear as a dominant variable in the system of equations. Since only the first derivatives of pressure with respect to each of the coordinates are nested in the system and not the second derivatives, it is difficult in primitive-variable solutions of the Navier-Stokes equations to maintain the elliptic character of the pressure field.

Consequently, in the present approach, the governing equations are solved in terms of a dimensionless compressible stream function ψ defined by

$$\frac{\partial \psi}{\partial y} = \bar{\rho} \tilde{u} \quad (7)$$

$$\frac{\partial \psi}{\partial x} = -\bar{\rho} \tilde{v} \quad (8)$$

and a dimensionless vorticity ω defined by

$$\omega = \frac{\partial \tilde{v}}{\partial x} - \frac{\partial \tilde{u}}{\partial y} \quad (9)$$

With this approach the stream function is computed from an equation derived by combining Equations (7) through (9), and the vorticity is computed from a transport equation derived by combining derivatives of the momentum equations in a manner that eliminates the pressure from the equation for ω .

The dimensionless governing equations in the present planar-flow analysis are given below:

Poisson equation for stream function:

$$\frac{\partial^2 \psi}{\partial x^2} - \frac{1}{\bar{\rho}} \frac{\partial \bar{\rho}}{\partial x} \frac{\partial \psi}{\partial x} + \frac{\partial^2 \psi}{\partial y^2} - \frac{1}{\bar{\rho}} \frac{\partial \bar{\rho}}{\partial y} \frac{\partial \psi}{\partial y} = -\bar{\rho} \omega \quad (10)$$

Transport equation for vorticity:

$$\tilde{\mu}_{\text{eff}} \left(\frac{\partial^2 \omega}{\partial x^2} + \frac{\partial^2 \omega}{\partial y^2} \right) + \left(2 \frac{\partial \tilde{\mu}_{\text{eff}}}{\partial x} - \text{Re} \frac{\partial \psi}{\partial y} \right) \frac{\partial \omega}{\partial x} + \left(2 \frac{\partial \tilde{\mu}_{\text{eff}}}{\partial y} + \text{Re} \frac{\partial \psi}{\partial x} \right) \frac{\partial \omega}{\partial y} = \text{Re} \phi_1 - \phi_2 - \frac{\text{Re}}{\text{Fr}^2} \frac{\partial \bar{\rho}}{\partial x}, \quad (11)$$

where $\tilde{\mu}_{\text{eff}}$ is the effective viscosity and the functions ϕ_1, ϕ_2 (as well as the functions ϕ_3 through ϕ_{13} which appear in subsequent equations) are defined in the Appendix. The boundary conditions on Equations (10) and (11) follow from known velocity distributions at the boundaries of the solution domain.

Poisson equation for static pressure:

$$\begin{aligned} \frac{\partial^2 \bar{p}}{\partial x^2} + \frac{\partial^2 \bar{p}}{\partial y^2} = \frac{2}{\text{Re}} \left(\frac{\partial^2 \tilde{\mu}_{\text{eff}}}{\partial x^2} \phi_3 + \frac{\partial \tilde{\mu}_{\text{eff}}}{\partial x} \phi_4 + 2 \frac{\partial^2 \tilde{\mu}_{\text{eff}}}{\partial x \partial y} \phi_5 + \frac{\partial \tilde{\mu}_{\text{eff}}}{\partial y} \phi_6 + \frac{\partial^2 \tilde{\mu}_{\text{eff}}}{\partial y^2} \phi_7 + \frac{4}{3} \tilde{\mu}_{\text{eff}} \phi_8 \right) \\ - 2\phi_9 + \frac{2}{\text{Fr}^2} \frac{\partial \bar{\rho}}{\partial y} - \frac{4}{3} \bar{\rho} \left(\frac{\partial^2 \bar{k}}{\partial x^2} + \frac{\partial^2 \bar{k}}{\partial y^2} \right) - \frac{4}{3} \bar{k} \left(\frac{\partial^2 \bar{\rho}}{\partial x^2} + \frac{\partial^2 \bar{\rho}}{\partial y^2} \right), \end{aligned} \quad (12)$$

where \bar{k} is the turbulent kinetic energy.

The boundary conditions on the pressure are determined through the pressure gradients imposed by the component momentum equations,

$$\frac{\partial \bar{p}}{\partial x} = \frac{2}{\text{Re}} \left(\frac{\partial \tilde{\mu}_{\text{eff}}}{\partial x} \phi_3 + \frac{\partial \tilde{\mu}_{\text{eff}}}{\partial y} \phi_5 + \frac{1}{2} \tilde{\mu}_{\text{eff}} \phi_4 \right) - 2\phi_{10} - \frac{4}{3} \left(\bar{\rho} \frac{\partial \bar{k}}{\partial x} + \bar{k} \frac{\partial \bar{\rho}}{\partial x} \right) \quad (13)$$

$$\frac{\partial \bar{p}}{\partial y} = \frac{2}{\text{Re}} \left(\frac{\partial \tilde{\mu}_{\text{eff}}}{\partial x} \phi_5 + \frac{\partial \tilde{\mu}_{\text{eff}}}{\partial y} \phi_7 + \frac{1}{2} \tilde{\mu}_{\text{eff}} \phi_6 \right) - 2\phi_{11} + \frac{2}{\text{Fr}^2} \bar{\rho} - \frac{4}{3} \left(\bar{\rho} \frac{\partial \bar{k}}{\partial y} + \bar{k} \frac{\partial \bar{\rho}}{\partial y} \right) \quad (14)$$

Transport equation for thermal energy:

$$\begin{aligned} \frac{1}{\text{Pr}} \frac{\tilde{k}_{\text{eff}}}{\tilde{c}_p} \left(\frac{\partial^2 \tilde{h}}{\partial x^2} + \frac{\partial^2 \tilde{h}}{\partial y^2} \right) + \left[\frac{1}{\text{Pr}} \frac{\partial}{\partial x} \left(\frac{\tilde{k}_{\text{eff}}}{\tilde{c}_p} \right) - \text{Re} \frac{\partial \psi}{\partial y} \right] \frac{\partial \tilde{h}}{\partial x} + \left[\frac{1}{\text{Pr}} \frac{\partial}{\partial y} \left(\frac{\tilde{k}_{\text{eff}}}{\tilde{c}_p} \right) + \text{Re} \frac{\partial \psi}{\partial x} \right] \frac{\partial \tilde{h}}{\partial y} \\ = \frac{\text{Re}}{2\bar{\rho}} \left(\frac{\partial \psi}{\partial x} \frac{\partial \bar{p}}{\partial y} - \frac{\partial \psi}{\partial y} \frac{\partial \bar{p}}{\partial x} \right) - \phi_{12} - \frac{\text{Re}}{\text{Fr}^2} \frac{\partial \psi}{\partial x} - \frac{2}{3} \frac{\text{Re} \bar{k}}{\bar{\rho}} \left(\frac{\partial \bar{\rho}}{\partial y} \frac{\partial \psi}{\partial x} - \frac{\partial \bar{\rho}}{\partial x} \frac{\partial \psi}{\partial y} \right), \end{aligned} \quad (15)$$

where \tilde{k}_{eff} is the effective thermal conductivity and \tilde{c}_p is the constant-pressure specific heat. The boundary conditions on the static enthalpy are determined through the temperature and heat flux distributions specified at the boundaries.

Transport equation for turbulent kinetic energy:

$$\begin{aligned} \tilde{\mu}_k \left(\frac{\partial^2 \bar{k}}{\partial x^2} + \frac{\partial^2 \bar{k}}{\partial y^2} \right) + \left(\frac{\partial \tilde{\mu}_k}{\partial x} - \text{Re} \frac{\partial \psi}{\partial y} \right) \frac{\partial \bar{k}}{\partial x} + \left(\frac{\partial \tilde{\mu}_k}{\partial y} + \text{Re} \frac{\partial \psi}{\partial x} \right) \frac{\partial \bar{k}}{\partial y} \\ = \text{Re} \left[-\frac{\phi_{13}}{\text{Re}} + \frac{2}{3} \frac{\bar{k}}{\bar{\rho}} \left(\frac{\partial \bar{\rho}}{\partial y} \frac{\partial \psi}{\partial x} - \frac{\partial \bar{\rho}}{\partial x} \frac{\partial \psi}{\partial y} \right) + \bar{\rho} \epsilon_d + \frac{2\tilde{\mu}}{\text{Re}} \left(\frac{\partial \sqrt{\bar{k}}}{\partial y} \right)^2 \right], \end{aligned} \quad (16)$$

where ϵ_d is the turbulent dissipation. Quantities used in the Jones-Launder two-equation turbulence model are defined in Equation (18).

Transport equation for turbulent dissipation:

$$\begin{aligned} \tilde{\mu}_e \left(\frac{\partial^2 \epsilon_d}{\partial x^2} + \frac{\partial^2 \epsilon_d}{\partial y^2} \right) + \left(\frac{\partial \tilde{\mu}_e}{\partial x} - \text{Re} \frac{\partial \psi}{\partial y} \right) \frac{\partial \epsilon_d}{\partial x} + \left(\frac{\partial \tilde{\mu}_e}{\partial y} + \text{Re} \frac{\partial \psi}{\partial x} \right) \frac{\partial \epsilon_d}{\partial y} = \text{Re} \left\{ -\frac{C_1 \epsilon_d}{k} \frac{\phi_{13}}{\text{Re}} + \frac{2}{3} \frac{C_1 \epsilon_d}{\bar{\rho}} \right. \\ \left. \left[\frac{\partial \psi}{\partial x} \frac{\partial \bar{\rho}}{\partial y} - \frac{\partial \bar{\rho}}{\partial x} \frac{\partial \psi}{\partial y} \right] - \frac{2 \tilde{\mu}_t}{\bar{\rho}^3 \text{Re}^2} \left[\frac{\partial^3 \psi}{\partial y^3} - \frac{2}{\bar{\rho}} \frac{\partial \bar{\rho}}{\partial y} \frac{\partial^2 \psi}{\partial y^2} + \frac{2}{\bar{\rho}^2} \frac{\partial \psi}{\partial y} \left(\frac{\partial \bar{\rho}}{\partial y} \right)^2 - \frac{1}{\bar{\rho}} \frac{\partial \psi}{\partial y} \frac{\partial^2 \bar{\rho}}{\partial y^2} \right]^2 + \frac{C_2 f_2 \bar{\rho} \epsilon_d^2}{k} \right\} \quad (17) \end{aligned}$$

Jones-Launder turbulence-model relations:

$$\left. \begin{aligned} f_2 &= 1 - 0.3e^{-R_t^2}, \quad \tilde{\mu}_t = \tilde{\mu}_c \mu f_\mu R_t \\ f_\mu &= \exp \left[\frac{-2.5}{1 + R_t/50} \right], \quad \tilde{\mu}_k = \tilde{\mu} + \lambda_k \tilde{\mu}_t \\ \tilde{\mu}_e &= \tilde{\mu} + \lambda_e \tilde{\mu}_t, \quad \tilde{\mu}_{\text{eff}} = \tilde{\mu} + \tilde{\mu}_t \\ \frac{\tilde{k}_{\text{eff}}}{\tilde{c}_p} &= \frac{\tilde{k}_{\text{mol}}}{\tilde{c}_p} + \tilde{\mu}_t \frac{Pr}{Pr_t}, \quad R_t = \text{Re} \frac{\bar{\rho} \tilde{k}^2}{\tilde{\mu} \epsilon_d} \\ \lambda_k &= 1, \lambda_e = 0.9091, Pr = 0.72, Pr_t = 0.9 \\ C_1 &= 1.44, C_2 = 1.92, c_\mu = 0.09 \end{aligned} \right\} \quad (18)$$

Either the turbulent kinetic energy and turbulent dissipation or their normal derivatives are specified at the boundaries.

The system of equations is completed with the equations of state,

$$\bar{p} = 2\bar{\rho} \left(\frac{\gamma - 1}{\gamma} \right) \tilde{h} \quad (19)$$

$$\tilde{h} = \tilde{c}_p \tilde{T}, \quad (20)$$

where γ is the ratio of specific heats and T is the static temperature, and with the temperature variation of the transport properties given by Worsøe-Schmidt and Leppert¹²,

$$\tilde{\mu} = \left(\frac{\tilde{h}}{\tilde{h}_0} \right)^{0.67} \quad (21)$$

$$\tilde{k}_{th} = \left(\frac{\tilde{h}}{\tilde{h}_0} \right)^{0.71} \quad (22)$$

Equations (10) through (22) contain the following parameters which appear as a result of the normalization: $Re = \bar{\rho}_0 \bar{V}_0 \bar{D} / \bar{\mu}_0$, the Reynolds number; $Fr = \bar{V}_0 / \sqrt{g_0 \bar{D}}$, the Froude number; and $Pr = \bar{c}_{p,0} \bar{\mu}_0 / \bar{k}_{th,0}$, the Prandtl number. The reference conditions, denoted by the subscript, 0, are taken to be the centerline values at the jet exit plane.

For the case of incompressible flow, $\rho = 1$, and the previous equations become greatly simplified both in form and number. The transport equation for thermal energy, the equations of state, and the temperature variations of the transport properties are not needed. In addition, the Poisson equations for static pressure need not be solved simultaneously with the Poisson equation for stream function and the vorticity transport equation.

2.2 The Numerical Solution Scheme

To solve the flowfield equations for a planar jet discharging from a curved upper surface, as shown in Figure 1, a conformal mapping technique is used to map the irregular physical plane into a rectangular computational plane. The governing equations are then rewritten in terms of the computational plane coordinates and solved using finite-difference procedures. Since there is geometric symmetry with respect to the jet centerline, only half of the flowfield need be treated.

The mapping technique, which is an inverse procedure, was devised at MDRL by G.H. Hoffman and is best explained with reference to Figure 3. Initially, a finite-difference computational plane with coordinates (ξ, η) is specified. The distance between nodes in the ξ direction is a and in the η direction is b , where a and b are not necessarily equal. Stretching functions can then be applied in each coordinate direction:

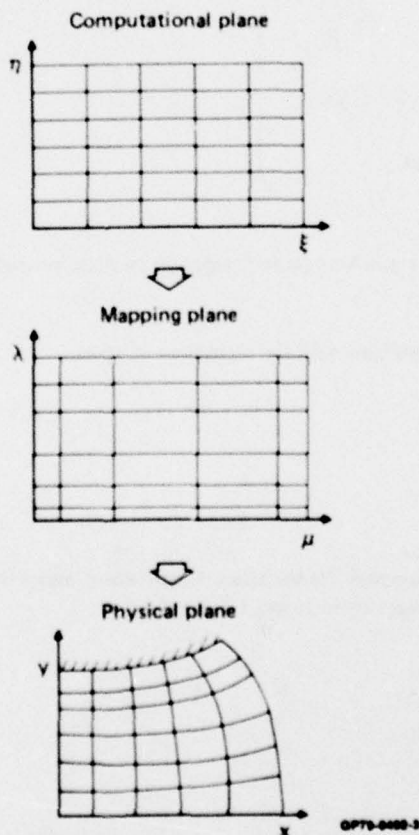


Figure 3. Inverse conformal mapping with stretching.

$$\mu = f_1(\xi), \quad (23)$$

and

$$\lambda = f_2(\eta). \quad (24)$$

With these relations, a mapping plane (μ, λ) is determined which permits finer resolution of the flowfield in regions where the gradients of the computed variables are severe. Finally, a conformal mapping given by

$$\mu + i\lambda = F(x + iy) \quad (25)$$

is introduced which specifies the physical plane (x, y) . Since the mapping [Equation (25)] holds, it follows that both x and y obey Laplace's equations with coordinate stretching

$$\frac{d\xi}{d\mu} \frac{\partial}{\partial \xi} \left(\frac{d\xi}{d\mu} \frac{\partial y}{\partial \xi} \right) + \frac{d\eta}{d\lambda} \frac{\partial}{\partial \eta} \left(\frac{d\eta}{d\lambda} \frac{\partial y}{\partial \eta} \right) = 0 \quad (26)$$

$$\frac{d\xi}{d\mu} \frac{\partial}{\partial \xi} \left(\frac{d\xi}{d\mu} \frac{\partial x}{\partial \xi} \right) + \frac{d\eta}{d\lambda} \frac{\partial}{\partial \eta} \left(\frac{d\eta}{d\lambda} \frac{\partial x}{\partial \eta} \right) = 0. \quad (27)$$

The boundary conditions imposed on Equations (26) and (27) follow from physical constraints when they are known at the boundaries, and from integration of the Cauchy-Riemann relations,

$$\frac{d\xi}{d\mu} \frac{\partial x}{\partial \xi} = \frac{d\eta}{d\lambda} \frac{\partial y}{\partial \eta}, \quad (28)$$

and

$$\frac{d\eta}{d\lambda} \frac{\partial x}{\partial \eta} = - \frac{d\xi}{d\mu} \frac{\partial y}{\partial \xi}, \quad (29)$$

when the x and y boundary distributions are not known.

The unique feature of the present mapping scheme is that instead of specifying the coordinate distributions in the physical plane and accepting whatever computational plane results, a numerically convenient computational plane is specified, and the corresponding coordinate distributions within the specified physical boundaries are computed. For this reason, the mapping scheme is an inverse procedure.

In the present analysis the mapping equations are discretized using conventional central-difference, finite-difference approximations to the derivatives. This discretization is not the case for the flowfield equations. The reason for this can be explained with reference to the following general form of the flowfield equations which appear in the analysis, where ϕ is an arbitrary flow variable, $\phi = \psi, \bar{p}, \omega, \tilde{h}, \tilde{k}$, or ϵ_d :

$$\alpha \frac{\partial^2 \phi}{\partial \xi^2} + \gamma \frac{\partial \phi}{\partial \xi} + \beta \frac{\partial^2 \phi}{\partial \eta^2} + \delta \frac{\partial \phi}{\partial \eta} = \sigma. \quad (30)$$

The coefficients α, γ, β , and δ and the source term σ are functions of the flow variables.

The central-difference, finite-difference algorithm applied to Equation (30) provides diagonal dominance and thereby convergent solutions for only a limited range in the magnitudes of the coefficients γ and δ . This range is generally exceeded in the transport equations in which γ and δ contain the Reynolds number as a multiplicative factor. To ensure diagonal dominance for all values of γ and δ , Hoffman's augmented-central-difference algorithm¹³ was applied to Equation (30). The central idea of this method can be explained by considering, for example, the derivative $\partial\phi/\partial\xi$. Using the point-of-the-compass notation shown in Figure 4 to designate the variable locations, this derivative can be evaluated at the central point P in terms of the adjacent east (E) and west (W) points with the following truncated Taylor-series representation and standard central-difference approximation to the first derivative:

$$\left. \frac{\partial\phi}{\partial\xi} \right|_P = \frac{\phi_E - \phi_W}{2a} - \frac{a^2}{6} \left. \frac{\partial^3\phi}{\partial\xi^3} \right|_P - \frac{a^4}{5!} \left. \frac{\partial^5\phi}{\partial\xi^5} \right|_P \quad (31)$$

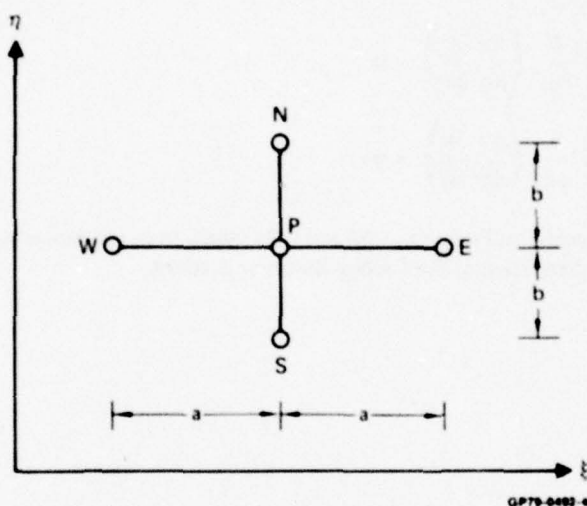


Figure 4. Five-point finite-difference stencil.

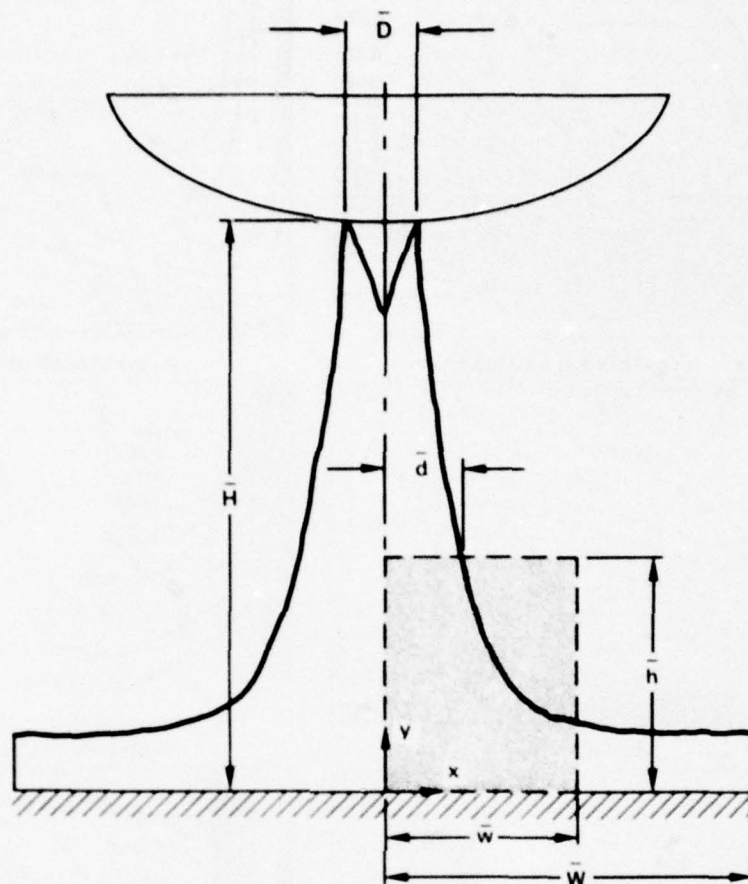
In the augmented-central-difference scheme, the derivative $\partial^3\phi/\partial\xi^3$ is retained and expressed in terms of lower-order derivatives by differentiating the governing transport equation with respect to ξ . The convective derivative $\partial\phi/\partial\eta$ is represented in an analogous fashion with the algorithm.

The finite-difference equations are solved using point relaxation. For each flow variable ϕ , a local residual is defined by $r_\phi = |\phi_{N+1} - \phi_N|$, where N is the iteration counter. Convergence is said to be achieved when $r_\phi < 10^{-6}$ everywhere in the flowfield.

2.3 The Computed Flowfields

The configuration considered first in the analysis is the planar impinging jet illustrated in Figure 1. However, in order to avoid the additional complexity of treating the irregular boundary of the undersurface from which the jet discharges, the top surface of the computational region, as shown in the shaded portion of Figure 5, was initially taken to be a distance \bar{h} above the ground plane. The right surface was taken to be a distance \bar{w} from the jet centerline. Since normal impingement is considered, geometric symmetry about the jet centerline exists so that only half the flowfield need be solved.

The required boundary conditions for this problem follow from known velocity and turbulence profiles at the top boundary of the computational region; from the no-slip, impermeable wall constraint at the ground plane; from symmetry at the jet centerline; and from the assumption of no gradients in the flow properties at the right boundary. Calculations were performed for the turbulent planar jet with Reynolds numbers of 1.46×10^4 and 1.27×10^5 based on the width of the jet \bar{d} at the top surface of the computational region and the jet centerline properties at the same station. The dimensions $h = \bar{h}/\bar{d} = 1$ and $w = \bar{w}/\bar{d} = 2.5$ were chosen. A finite-difference mesh was used with 51 nodes in the x direction and 41 in the y direction.



GP79-0779-29

Figure 5. Definition of the computational region for the free-upper-boundary planar impinging jet.

Computed flow variables for this configuration with $Re = 1.27 \times 10^5$ are illustrated in the contour plots of Figure 6. The characteristic features of the planar impinging jet are clearly shown. The stream function distribution demonstrates the circulation zone in the top region of the flowfield and jet turning near the ground, and the vorticity distribution demonstrates the convection of ω toward the right boundary with the development of a wall jet along the lower surface. The entrainment and wall jet characteristics are further illustrated by the contour of the x-component of velocity, and the rate of decay of jet centerline velocity is illustrated by the contour of the y-component of velocity. The static pressure contour shows the strong pressure gradients experienced in both coordinate directions when proceeding toward the stagnation point, a feature which precludes the use of conventional boundary-layer theory in modeling the viscous effects of an impinging jet flow. The turbulence field is illustrated by the contour plots of the turbulent kinetic energy, the turbulent dissipation, and the length scale. The latter is computed from the relation $L = k^{1.5}/\epsilon_d$, which further reflects the relative turbulence levels in the flowfield.

The corresponding contour plots for the planar jet with $Re = 1.46 \times 10^4$ are not shown since they demonstrate the same qualitative behavior as those given for $Re = 1.27 \times 10^5$ in Figure 6. Figure 7 contains comparisons of the measured and computed ground-plane pressure distributions using the data of Schauer and Eustis¹⁴ for $Re = 1.27 \times 10^5$ and the data of Gardon and Akfirat¹⁵ for $Re = 1.46 \times 10^4$.

In calculating the flowfields for the planar impinging jet with a confining upper surface, the computational region shown in Figure 8 was used. The solution domain has a height H and a width W , where both dimensions are normalized by the jet width.

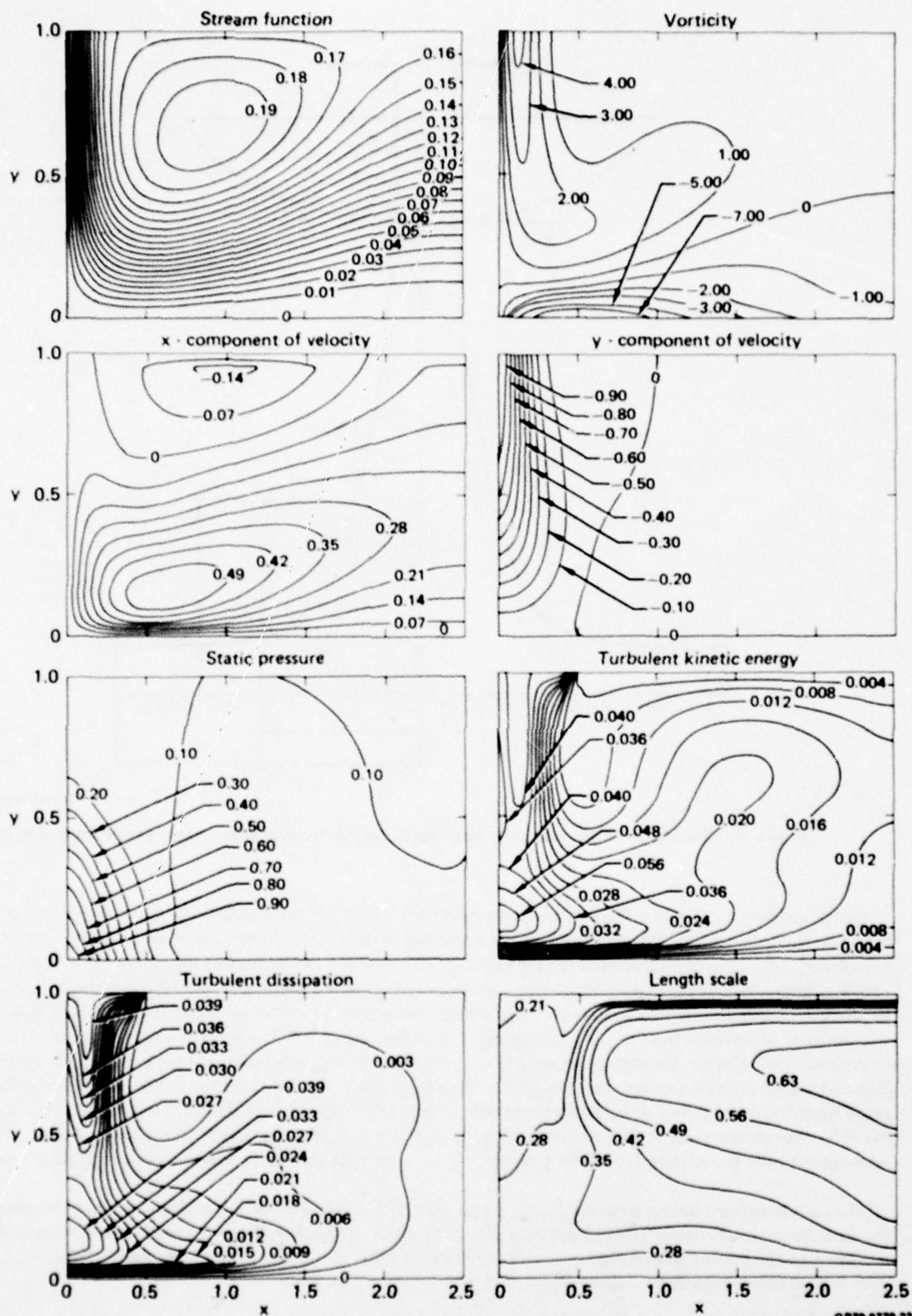


Figure 6. Property contours for the incompressible free-upper-boundary planar jet in ground effect ($h = 1$, $w = 2.5$, $Re = 1.27 \times 10^5$).

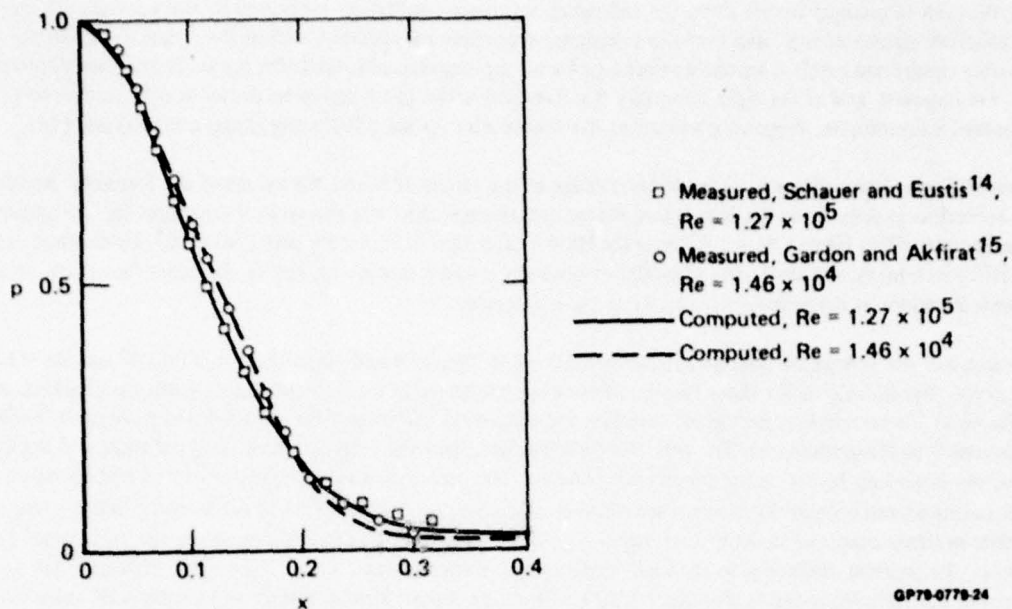


Figure 7. Comparison of experimental and theoretical ground-plane pressure distributions for the normal impingement of the free-upper-boundary planar jet with a fully developed profile.

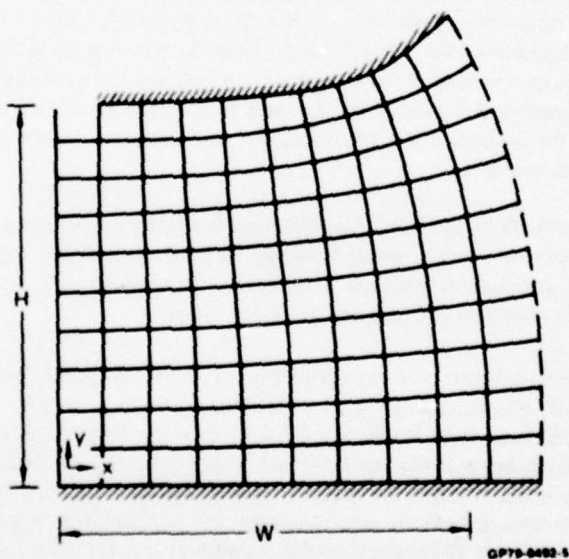


Figure 8. Definition of the computational region in the physical plane for a simulated fuselage undersurface in ground effect.

For the case of incompressible flow, the following boundary conditions are imposed: the vorticity, stream function, turbulent kinetic energy, and turbulent dissipation profiles are specified within the entering jet. On the solid boundaries conditions result from the constraint of a no-slip impermeable wall. On the jet centerline symmetry conditions are imposed, and at the right boundary the flow properties are taken to be uniform with respect to ξ , the transformed x coordinate. Pressure gradients at the boundaries are specified using Equations (13) and (14).

Flowfield calculations have been made for a range in the values of H and the values of the Reynolds number based on jet centerline properties at the exit plane. Representative solutions are shown in this section for the upper surface in close ground effect ($H = 2$, $W = 3.68$) and for $Re = 1.00 \times 10^2$, 1.00×10^4 , and 1.30×10^5 . In the first case a finite-difference mesh was used with 41 nodes in both the x and y directions, and in the latter two cases a mesh was used with 81 nodes in the x direction and 41 in the y direction.

Contours of the computed fluid properties are shown in Figures 9 and 10 for $Re = 1.00 \times 10^2$ and $Re = 1.30 \times 10^5$, respectively. The flowfields for these two conditions are qualitatively similar, and their significant characteristics are the following: the stream function plots illustrate the turning of the jet and the recirculation pattern, including entrainment into the primary jet. The vorticity distributions show the convection of ω to the right and the development of the boundary layers on the upper wall (where separation occurs at the point of $\omega = 0$) and on the lower wall. The entrainment and recirculation zones are more clearly illustrated in the plots of the x - and y -velocity components. The static pressure contours show an increase in p going toward the stagnation point where the value is set to unity. Of course, the greatest difference in the high- and low-Reynolds number solutions shown in Figures 9 and 10 is reflected in the turbulence fields. For $Re = 1.30 \times 10^5$ the turbulent kinetic energy and length scale values are much larger in the recirculation zone than they are for $Re = 1.00 \times 10^2$.

The contour plots for the planar jet with $Re = 1.00 \times 10^4$ are not shown since they have the same qualitative characteristics as those for $Re = 1.30 \times 10^5$. A comparison of the computed and measured pressure variations for the ground plane and simulated fuselage undersurface is shown in Figure 11 for the Reynolds number range with $H = 2$ and $W = 3.68$. The data, which were obtained in a test program described in Ref. 16, were measured with $Re = 1.30 \times 10^5$, while the computed values correspond to $Re = 1.00 \times 10^2$, $Re = 1.00 \times 10^4$, and $Re = 1.30 \times 10^5$. The influence of Reynolds number on the solution results from the role it plays in determining the turbulent entrainment into the primary jet. A comparison of the computed and measured jet centerline turbulent-kinetic-energy and velocity distributions is illustrated in Figure 12 for the same geometry and values of Re . The agreement is good except in the proximity of the wall where the Jones-Launder turbulence model given by Equations (16) - (18) fails to provide the observed variation of k .

For the case of compressible flow, the following additional boundary conditions are imposed to determine the transport equation for the thermal energy: within the entering jet the enthalpy profile is specified; the upper surface is assumed to be isothermal, and the lower surface is assumed to be adiabatic; and on the jet centerline and at the right boundary, the enthalpy gradients with respect to ξ are set to zero.

Figure 13 shows the various contour plots calculated for the planar compressible jet in ground effect with $H = 2$, $W = 3.68$, $Re = 1.00 \times 10^2$, $Pr = 0.68$, and $Fr = 1.63 \times 10^2$. The stream-function, vorticity, and velocity-component profiles demonstrate the same basic form for the compressible case as for the incompressible case. The static pressure profile is also of the same form, but p at the stagnation point is not set to unity since its value is fixed by the equation of state. The static enthalpy contour shows the decay in temperature with distance from the jet core, and the density distribution reflects the variations in both the static enthalpy and pressure, with ρ increasing toward the upper boundary where the temperature is lowest. The k and ϵ profiles (the latter is not shown) have the same qualitative characteristics as for the case of incompressible flow, which is expected from the Morkovin hypothesis.

Higher-Reynolds-number calculations using the Jones-Launder turbulence model were not carried out for the compressible planar jet because of grid-size limitations imposed by the storage capacity of the CDC CYBER 175 used in the computations. These calculations must be performed on a computer which has a larger storage capacity and will thereby permit accurate computations at higher Reynolds numbers.

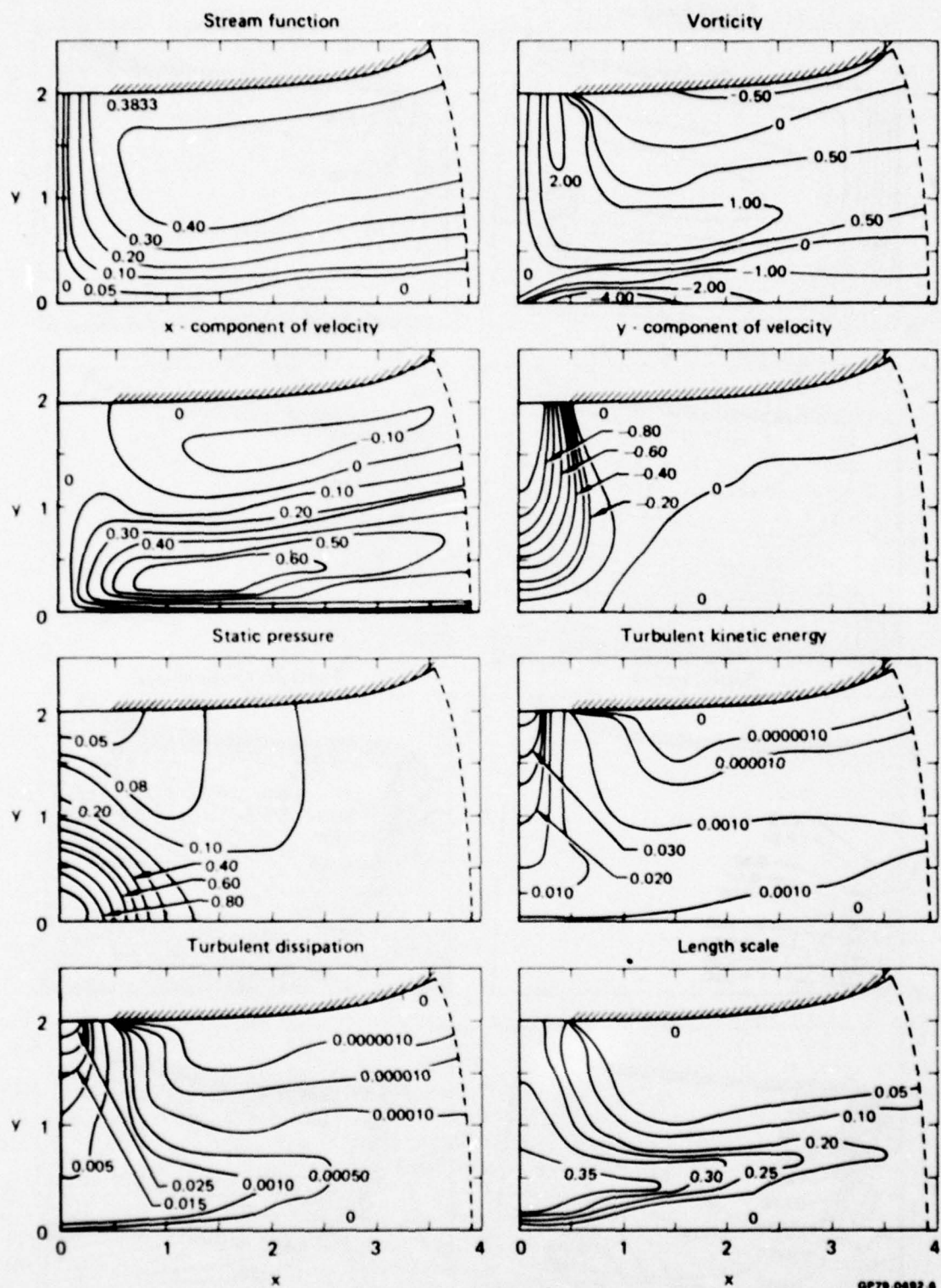
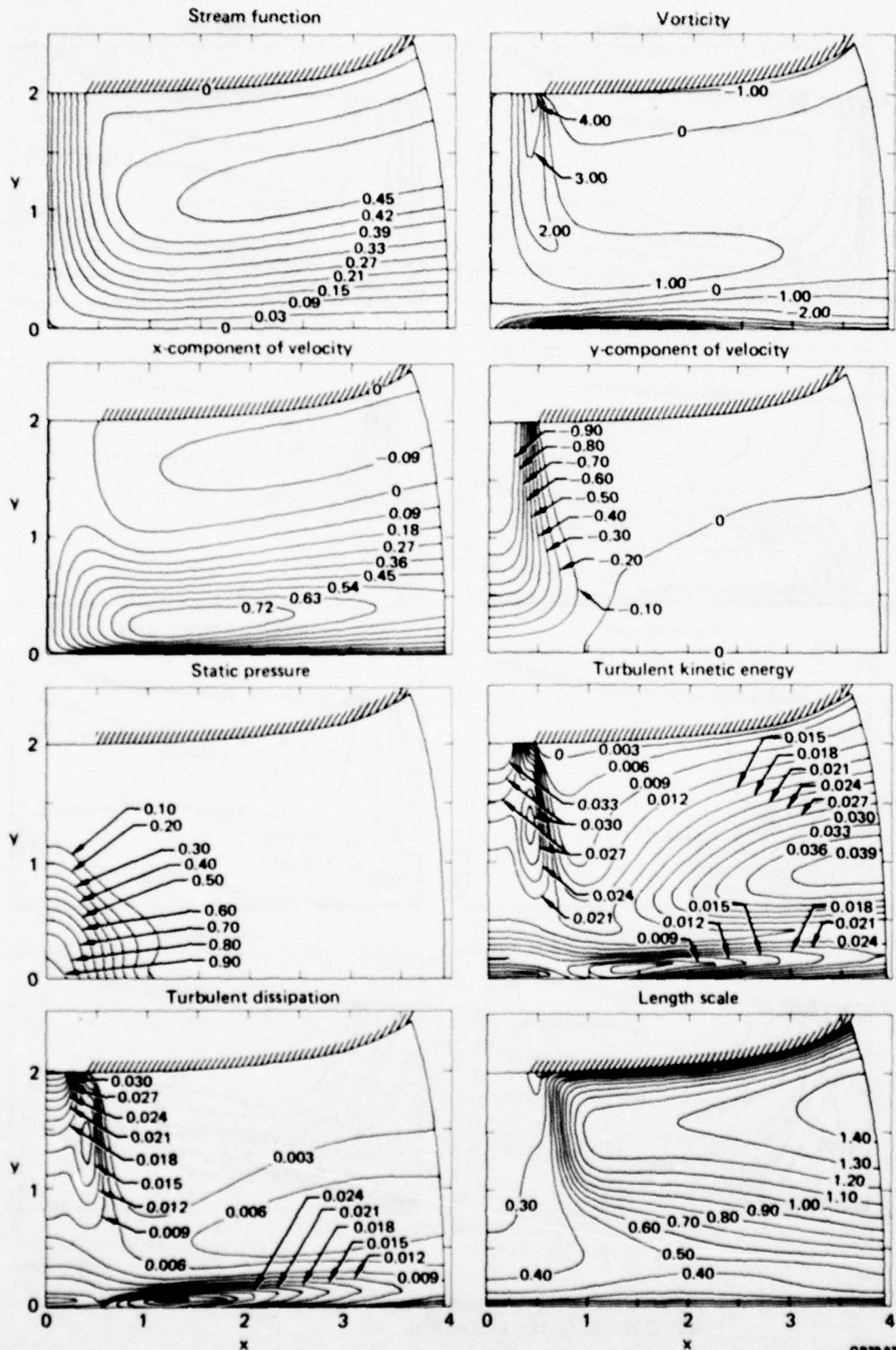
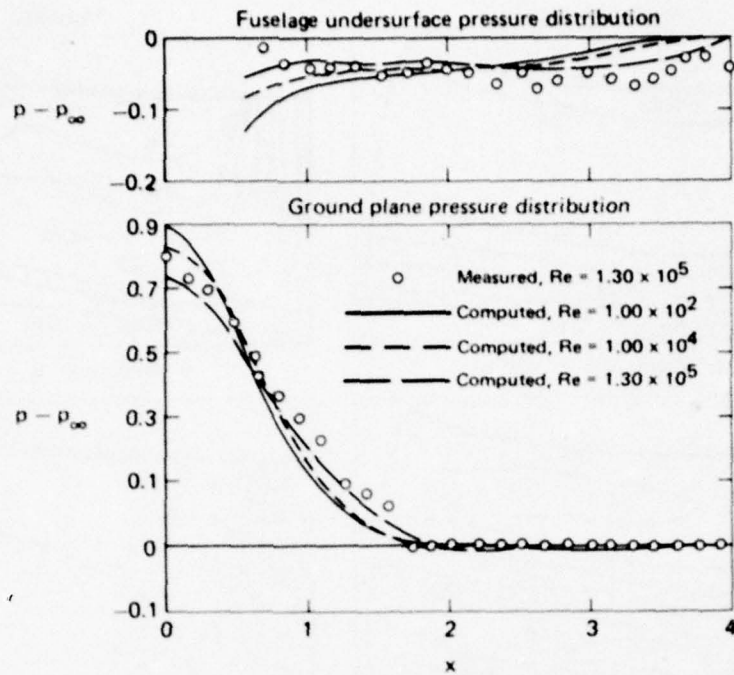


Figure 9. Property contours for the incompressible planar jet in ground effect ($H = 2$, $W = 3.68$, $Re = 1.00 \times 10^2$).



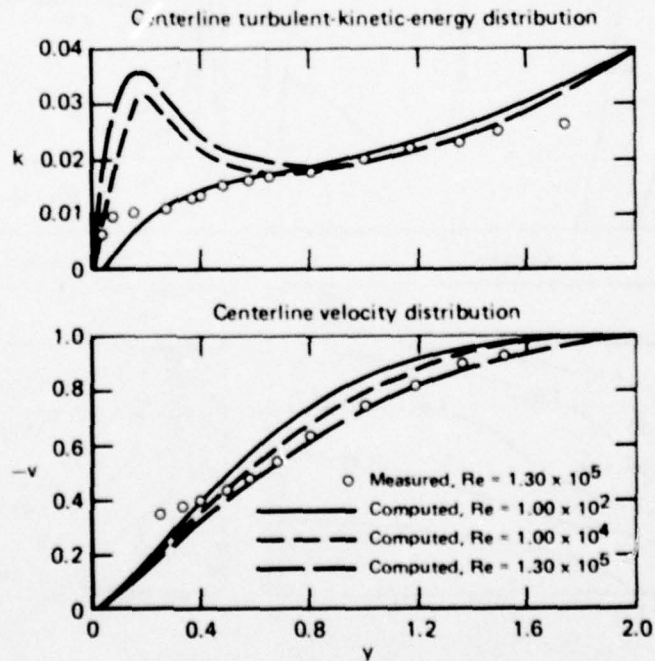
GP79-0779-25

Figure 10. Property contours for the incompressible planar jet in ground effect ($H = 2$, $W = 3.68$, $Re = 1.30 \times 10^5$).



GP79-0779-30

Figure 11. Comparison of experimental and theoretical pressure distributions for the incompressible planar jet in ground effect ($H = 2$, $W = 3.68$).



GP79-0779-26

Figure 12. Comparison of experimental and theoretical centerline property distributions for the incompressible planar jet in ground effect ($H = 2$, $W = 3.68$).

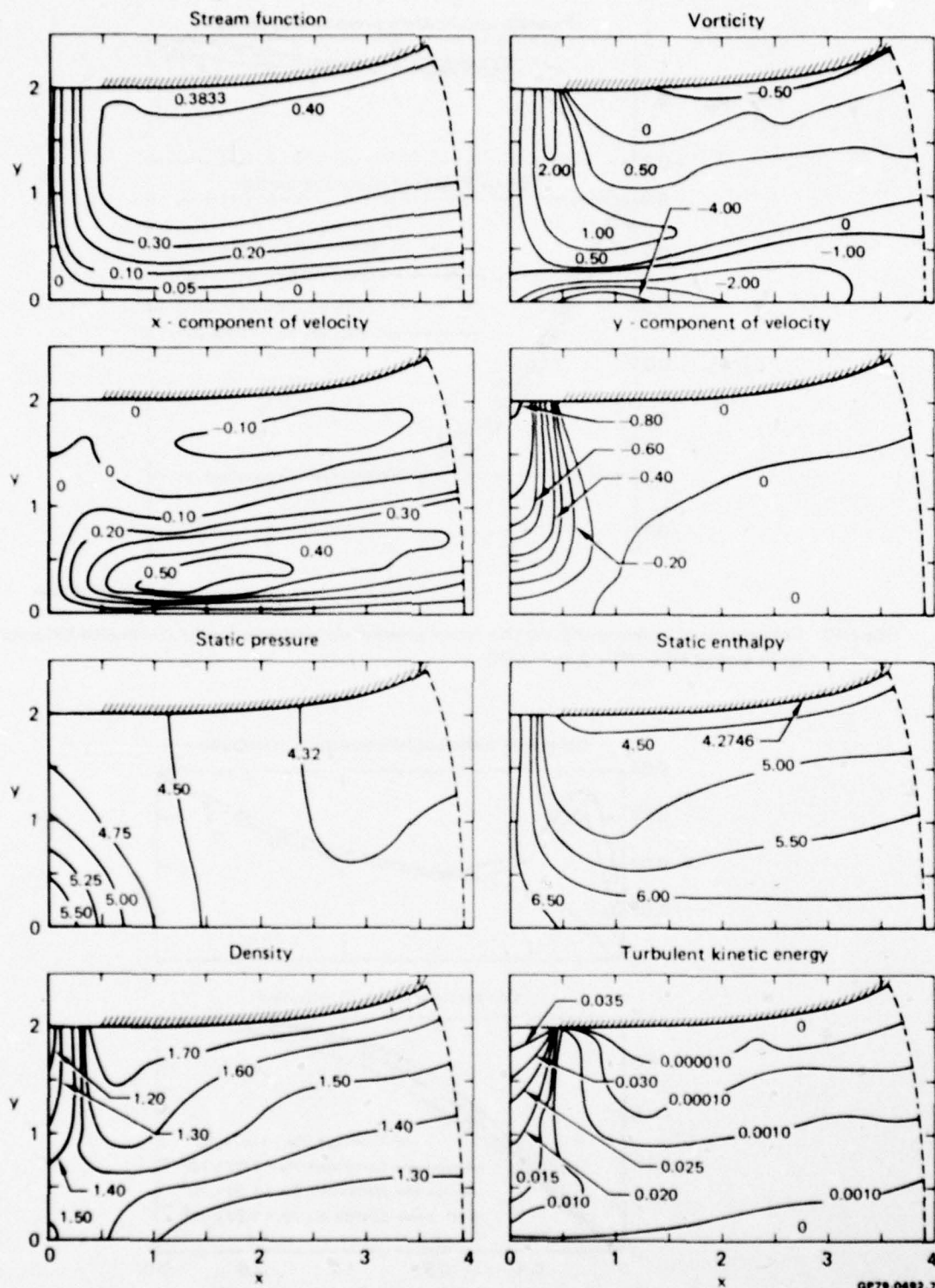


Figure 13. Property contours for the compressible planar jet in ground effect
 $(H = 2, W = 3.68, Re = 1.00 \times 10^2, Pr = 0.68, Fr = 1.63 \times 10^2)$.

3. ANALYSIS OF THREE-DIMENSIONAL IMPINGING JETS

In this section the procedure is described for computing the incompressible turbulent flowfield resulting from two interacting, initially axisymmetric jets with fountain formation as shown in Figure 2. Contour plots of the calculated flow variables are presented.

3.1 The Governing Equations

The time-averaged continuity and momentum equations which form the starting point in the three-dimensional, steady, incompressible flow analysis are Equations (1) and (2), which can be simplified with the condition of constant density. Turbulence closure is obtained by modeling the Reynolds stress term using the Glushko-Rubesin one-equation model for incompressible flow. A two-equation turbulence model is currently not used in the three-dimensional analysis because of storage limitations imposed by the CYBER 175 computer.

Equations (1) and (2) are expanded from tensor notation into cartesian coordinates (x, y, z) with the corresponding velocity components (u, v, w) , but the equations are not solved in primitive-variable form. Rather, a potential-function/vorticity approach first proposed by Aregbesola and Burley¹⁷ is adopted. In this technique, which is analogous to the stream-function/vorticity representation of the two-dimensional problem, the pressure is eliminated from the momentum equations in the formulation of a vorticity transport equation. The pressure field is then computed from a Poisson equation derived from the derivatives of the component momentum equations.

To identically satisfy the continuity condition, a scalar potential Φ and a vector potential A_i are introduced and the velocity field is given as

$$u_i = -\frac{\partial \Phi}{\partial x_i} + \epsilon_{ijk} \frac{\partial A_k}{\partial x_j} \quad (32)$$

where ϵ_{ijk} is the alternating tensor. Hirasaki and Hellums¹⁸ have shown that a unique vector potential A_i , within the gradient of an arbitrary harmonic function, exists such that

$$\frac{\partial A_i}{\partial x_i} = 0. \quad (33)$$

A differential equation for the vector potential is derived by taking the curl of Equation (32) and using Equation (33), which gives

$$\frac{\partial^2 A_i}{\partial x_j \partial x_j} = -\Omega_i, \quad (34)$$

where the vorticity is defined by

$$\Omega_i = \epsilon_{ijk} \frac{\partial u_k}{\partial x_j} \quad (35)$$

A differential equation for the scalar potential is derived by taking the divergence of Equation (32),

$$\frac{\partial^2 \Phi}{\partial x_i \partial x_i} = 0. \quad (36)$$

The advantage of introducing a scalar potential is the convenience it offers in setting the boundary conditions on the velocity components. Since Equation (36) is independent of Reynolds number, it need be solved only once for a given geometry and set of boundary conditions.

The boundary values of the vorticity are evaluated from Equation (35), where u_i is calculated from Equation (32). The boundary conditions on A_i are chosen such that its tangential components are equal to zero; the conditions on the normal components are then determined by Equation (33). For a flat boundary the conditions become

$$\frac{\partial A_n}{\partial n} = 0, A_t = 0, \quad (37)$$

where n denotes the normal component and t the tangential. The normal velocity components are assumed to be known, and these values are used to compute the normal derivatives of the scalar potential on the boundary,

$$\frac{\partial \Phi}{\partial n} = -n_i u_i. \quad (38)$$

The dimensionless governing equations in the present three-dimensional flow analysis are given below. Poisson equation for scalar potential:

$$\frac{\partial^2 \Phi}{\partial x^2} + \frac{\partial^2 \Phi}{\partial y^2} + \frac{\partial^2 \Phi}{\partial z^2} = 0 \quad (39)$$

Poisson equation for x component of vector potential:

$$\frac{\partial^2 A_x}{\partial x^2} + \frac{\partial^2 A_x}{\partial y^2} + \frac{\partial^2 A_x}{\partial z^2} = -\Omega_x \quad (40)$$

Poisson equation for y component of vector potential:

$$\frac{\partial^2 A_y}{\partial x^2} + \frac{\partial^2 A_y}{\partial y^2} + \frac{\partial^2 A_y}{\partial z^2} = -\Omega_y \quad (41)$$

Poisson equation for z component of vector potential:

$$\frac{\partial^2 A_z}{\partial x^2} + \frac{\partial^2 A_z}{\partial y^2} + \frac{\partial^2 A_z}{\partial z^2} = -\Omega_z \quad (42)$$

Transport equation for x component of vorticity:

$$\begin{aligned}
 [1 + \epsilon(\bar{r})] & \left(\frac{\partial^2 \Omega_x}{\partial x^2} + \frac{\partial^2 \Omega_x}{\partial y^2} + \frac{\partial^2 \Omega_x}{\partial z^2} \right) + \text{Re} \left[\frac{1}{\text{Re}} \frac{\partial \epsilon(\bar{r})}{\partial x} - u \right] \frac{\partial \Omega_x}{\partial x} + \text{Re} \left[\frac{1}{\text{Re}} \frac{\partial \epsilon(\bar{r})}{\partial y} - v \right] \frac{\partial \Omega_x}{\partial y} \\
 & + \text{Re} \left[\frac{1}{\text{Re}} \frac{\partial \epsilon(\bar{r})}{\partial z} - w \right] \frac{\partial \Omega_x}{\partial z} = \text{Re} \left[\left(\frac{\partial v}{\partial y} + \frac{\partial w}{\partial z} \right) \Omega_x + \frac{\partial u}{\partial y} \frac{\partial w}{\partial x} - \frac{\partial u}{\partial z} \frac{\partial v}{\partial x} \right] \\
 & + \left[- \frac{\partial^2 \epsilon(\bar{r})}{\partial x \partial y} \left(\frac{\partial w}{\partial x} + \frac{\partial u}{\partial z} \right) - 2 \frac{\partial^2 \epsilon(\bar{r})}{\partial y \partial z} \left(\frac{\partial w}{\partial z} - \frac{\partial v}{\partial y} \right) - \frac{\partial^2 \epsilon(\bar{r})}{\partial y^2} \left(\frac{\partial w}{\partial y} + \frac{\partial v}{\partial z} \right) \right. \\
 & - \frac{\partial \epsilon(\bar{r})}{\partial y} \left(\frac{\partial^2 w}{\partial x^2} + \frac{\partial^2 w}{\partial y^2} + \frac{\partial^2 w}{\partial z^2} \right) + \frac{\partial \epsilon(\bar{r})}{\partial z} \left(\frac{\partial^2 v}{\partial x^2} + \frac{\partial^2 v}{\partial y^2} + \frac{\partial^2 v}{\partial z^2} \right) \\
 & \left. + \frac{\partial^2 \epsilon(\bar{r})}{\partial x \partial z} \left(\frac{\partial v}{\partial x} + \frac{\partial u}{\partial y} \right) + \frac{\partial^2 \epsilon(\bar{r})}{\partial z^2} \left(\frac{\partial w}{\partial y} + \frac{\partial v}{\partial z} \right) \right] \quad (43)
 \end{aligned}$$

Transport equation for y component of vorticity:

$$\begin{aligned}
 [1 + \epsilon(\bar{r})] & \left(\frac{\partial^2 \Omega_y}{\partial x^2} + \frac{\partial^2 \Omega_y}{\partial y^2} + \frac{\partial^2 \Omega_y}{\partial z^2} \right) + \text{Re} \left[\frac{1}{\text{Re}} \frac{\partial \epsilon(\bar{r})}{\partial x} - u \right] \frac{\partial \Omega_y}{\partial x} + \text{Re} \left[\frac{1}{\text{Re}} \frac{\partial \epsilon(\bar{r})}{\partial y} - v \right] \frac{\partial \Omega_y}{\partial y} \\
 & + \text{Re} \left[\frac{1}{\text{Re}} \frac{\partial \epsilon(\bar{r})}{\partial z} - w \right] \frac{\partial \Omega_y}{\partial z} = \text{Re} \left[\left(\frac{\partial u}{\partial x} + \frac{\partial w}{\partial z} \right) \Omega_y + \frac{\partial v}{\partial z} \frac{\partial u}{\partial y} - \frac{\partial v}{\partial x} \frac{\partial w}{\partial y} \right] + \left[\frac{\partial^2 \epsilon(\bar{r})}{\partial x \partial y} \left(\frac{\partial w}{\partial y} + \frac{\partial v}{\partial z} \right) \right. \\
 & - \frac{\partial^2 \epsilon(\bar{r})}{\partial y \partial z} \left(\frac{\partial v}{\partial x} + \frac{\partial u}{\partial y} \right) + \frac{\partial^2 \epsilon(\bar{r})}{\partial x^2} \left(\frac{\partial w}{\partial x} + \frac{\partial u}{\partial z} \right) + \frac{\partial \epsilon(\bar{r})}{\partial x} \left(\frac{\partial^2 w}{\partial x^2} + \frac{\partial^2 w}{\partial y^2} + \frac{\partial^2 w}{\partial z^2} \right) \\
 & \left. - \frac{\partial \epsilon(\bar{r})}{\partial z} \left(\frac{\partial^2 u}{\partial x^2} + \frac{\partial^2 u}{\partial y^2} + \frac{\partial^2 u}{\partial z^2} \right) - 2 \frac{\partial^2 \epsilon(\bar{r})}{\partial x \partial z} \left(\frac{\partial u}{\partial x} - \frac{\partial w}{\partial z} \right) - \frac{\partial^2 \epsilon(\bar{r})}{\partial z^2} \left(\frac{\partial w}{\partial x} + \frac{\partial u}{\partial z} \right) \right] \quad (44)
 \end{aligned}$$

Transport equation for z component of vorticity:

$$\begin{aligned}
 [1 + \epsilon(\bar{r})] & \left(\frac{\partial^2 \Omega_z}{\partial x^2} + \frac{\partial^2 \Omega_z}{\partial y^2} + \frac{\partial^2 \Omega_z}{\partial z^2} \right) + \text{Re} \left[\frac{1}{\text{Re}} \frac{\partial \epsilon(\bar{r})}{\partial x} - u \right] \frac{\partial \Omega_z}{\partial x} + \text{Re} \left[\frac{1}{\text{Re}} \frac{\partial \epsilon(\bar{r})}{\partial y} - v \right] \frac{\partial \Omega_z}{\partial y} \\
 & + \text{Re} \left[\frac{1}{\text{Re}} \frac{\partial \epsilon(\bar{r})}{\partial z} - w \right] \frac{\partial \Omega_z}{\partial z} = \text{Re} \left[\left(\frac{\partial u}{\partial x} + \frac{\partial v}{\partial y} \right) \Omega_z + \frac{\partial w}{\partial x} \frac{\partial v}{\partial z} - \frac{\partial w}{\partial y} \frac{\partial u}{\partial z} \right] + \left[- \frac{\partial^2 \epsilon(\bar{r})}{\partial x^2} \left(\frac{\partial v}{\partial x} + \frac{\partial u}{\partial y} \right) \right. \\
 & - \frac{\partial \epsilon(\bar{r})}{\partial x} \left(\frac{\partial^2 v}{\partial x^2} + \frac{\partial^2 v}{\partial y^2} + \frac{\partial^2 v}{\partial z^2} \right) - 2 \frac{\partial^2 \epsilon(\bar{r})}{\partial x \partial y} \left(\frac{\partial v}{\partial y} - \frac{\partial u}{\partial x} \right) + \frac{\partial \epsilon(\bar{r})}{\partial y} \left(\frac{\partial^2 u}{\partial x^2} + \frac{\partial^2 u}{\partial y^2} + \frac{\partial^2 u}{\partial z^2} \right) \\
 & \left. - \frac{\partial^2 \epsilon(\bar{r})}{\partial x \partial z} \left(\frac{\partial w}{\partial y} + \frac{\partial v}{\partial z} \right) + \frac{\partial^2 \epsilon(\bar{r})}{\partial y^2} \left(\frac{\partial v}{\partial x} + \frac{\partial u}{\partial y} \right) + \frac{\partial^2 \epsilon(\bar{r})}{\partial y \partial z} \left(\frac{\partial w}{\partial x} + \frac{\partial u}{\partial z} \right) \right] \quad (45)
 \end{aligned}$$

Transport equation for turbulent kinetic energy:

$$\begin{aligned}
 [1 + \epsilon(\lambda \bar{r})] \left(\frac{\partial^2 k}{\partial x^2} + \frac{\partial^2 k}{\partial y^2} + \frac{\partial^2 k}{\partial z^2} \right) + \text{Re} \left[\frac{1}{\text{Re}} \frac{\partial \epsilon(\lambda \bar{r})}{\partial x} - u \right] \frac{\partial k}{\partial x} + \text{Re} \left[\frac{1}{\text{Re}} \frac{\partial \epsilon(\lambda \bar{r})}{\partial y} - v \right] \frac{\partial k}{\partial y} \\
 + \text{Re} \left[\frac{1}{\text{Re}} \frac{\partial \epsilon(\lambda \bar{r})}{\partial z} - w \right] \frac{\partial k}{\partial z} = \frac{Ck [1 + \epsilon(\lambda \bar{r})]}{L^2} - \epsilon(\bar{r}) \left[2 \frac{\partial u}{\partial x} \frac{\partial u}{\partial x} + \left(\frac{\partial v}{\partial x} + \frac{\partial u}{\partial y} \right) \frac{\partial u}{\partial y} + \left(\frac{\partial w}{\partial x} + \frac{\partial u}{\partial z} \right) \frac{\partial u}{\partial z} \right. \\
 \left. + \left(\frac{\partial v}{\partial x} + \frac{\partial u}{\partial y} \right) \frac{\partial v}{\partial x} + 2 \frac{\partial v}{\partial y} \frac{\partial v}{\partial y} + \left(\frac{\partial w}{\partial y} + \frac{\partial v}{\partial z} \right) \frac{\partial v}{\partial z} + \left(\frac{\partial w}{\partial x} + \frac{\partial u}{\partial z} \right) \frac{\partial w}{\partial x} + \left(\frac{\partial w}{\partial y} + \frac{\partial v}{\partial z} \right) \frac{\partial w}{\partial y} + 2 \frac{\partial w}{\partial z} \frac{\partial w}{\partial z} \right],
 \end{aligned} \quad (46)$$

where

$$\epsilon(\bar{r}) = H(\bar{r}) \alpha \bar{r} \quad (47)$$

and

$$H(\bar{r}) = \begin{cases} \frac{\bar{r}}{\bar{r}_0} & 0 \leq \frac{\bar{r}}{\bar{r}_0} < 0.75 \\ \frac{\bar{r}}{\bar{r}_0} - \left(\frac{\bar{r}}{\bar{r}_0} - 0.75 \right)^2 & 0.75 \leq \frac{\bar{r}}{\bar{r}_0} < 1.25 \\ 1 & 1.25 \leq \frac{\bar{r}}{\bar{r}_0} < \infty \end{cases} \quad (48)$$

The constants α , \bar{r}_0 , C , and λ have the values of 0.2, 110, 3.93, and 0.4, respectively, and the Reynolds number of the turbulence \bar{r} is defined by

$$\bar{r} = \frac{\sqrt{k} L}{\nu} \quad (49)$$

The length-scale distribution L must be specified throughout the flowfield.

The Reynolds number is based on jet centerline properties at the entrance plane to the solution domain.

3.2 The Numerical Solution Scheme

In the solution of the flowfield equations for two interacting, initially axisymmetric jets impinging perpendicularly on the ground, a conformal mapping is not required since the computational domain has no irregular boundaries. The governing equations can then be written in either one of the two forms given below.

Poisson equation:

$$\frac{\partial^2 \phi}{\partial x^2} + \frac{\partial^2 \phi}{\partial y^2} + \frac{\partial^2 \phi}{\partial z^2} = \sigma_1 \quad (50)$$

Transport equation:

$$\alpha \left(\frac{\partial^2 \phi}{\partial x^2} + \frac{\partial^2 \phi}{\partial y^2} + \frac{\partial^2 \phi}{\partial z^2} \right) + \text{Re } \beta \frac{\partial \phi}{\partial x} + \text{Re } \gamma \frac{\partial \phi}{\partial y} + \text{Re } \delta \frac{\partial \phi}{\partial z} = \text{Re } \sigma_2 + \sigma_3, \quad (51)$$

where ϕ denotes a general flow variable and $\alpha, \beta, \gamma, \delta, \sigma_1, \sigma_2$, and σ_3 denote general coefficients.

The Poisson equations are discretized using the conventional central-difference algorithm, but for the reason discussed in the section on the planar jet, the transport equations are discretized using the augmented-central-difference algorithm due to Hoffman¹³.

The coupled system of equations is solved iteratively using Gauss-Seidel line relaxation, where optimum relaxation factors were determined on the basis of numerical experimentation. As in the planar flow analysis, the convergence criterion for each variable ϕ is based on a residual $r_\phi = |\phi_{N+1} - \phi_N| < 10^{-6}$, where N is the iteration counter.

3.3 The Computed Flowfields

Incompressible flowfields have been calculated for the three-dimensional jet configuration of Figure 2 using the computational domain shown in Figure 14. The dimensions of the solution domain are normalized by the jet diameter d at the entrance plane to the computational region. The top surface of the latter is taken to be at a distance $H - h$ below the jet exit plane rather than at the exit plane in order to decrease the size of the computational region. Three of the side surfaces are jet symmetry planes; the additional symmetry-plane cut through the fountain ($z = 0$) is not made so that jets with unequal thrust levels can be treated later by the same computational scheme.

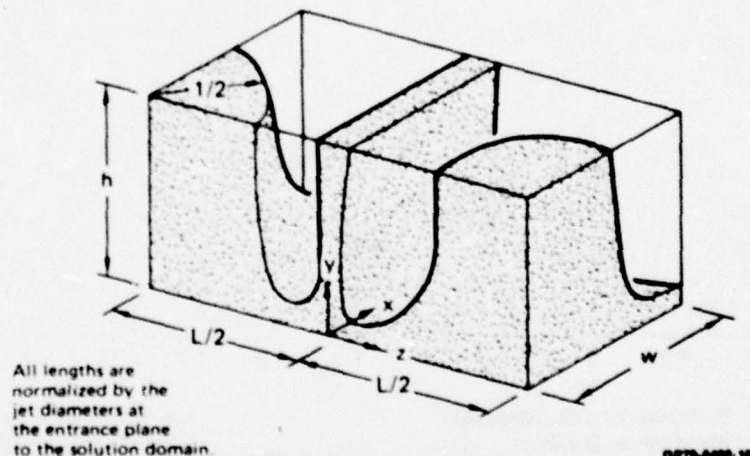


Figure 14. Definition of the computational region for two interacting, initially axisymmetric jets impinging perpendicularly on the ground with fountain formation.

Boundary conditions for this problem are determined from the no-slip, impermeable-wall constraints, symmetry conditions, and experimentally determined inflow/outflow velocity profiles. Turbulent-flow calculations were made with $L = 3$, $h = 1$, $w = 1$, and $\text{Re} = 1.00 \times 10^2$. In setting the finite-difference grid, 9 nodal points were used in the x direction, 9 in the y direction, and 25 in the z direction. Use of the CDC 7600 in future work will permit a greater number of nodes and thereby accurate calculations at higher Reynolds numbers.

Figure 15 shows representative flowfield contours in various planes of the computational region shown in Figure 14. Plots such as these reflect the desired symmetry maintained in the calculations and provide the basic data required to evaluate entrainment rates and fountain properties. However, these planar contour plots, even in large number (which are easily generated using an automated plotting procedure), do not provide a simple visualization of the overall flow patterns.

The physical characteristics of the flowfield are best illustrated through three-dimensional, particle-pathline traces, as shown in Figure 16. These plots are constructed in the following manner: after obtaining a convergent solution of the Navier-Stokes equations, the three components of the velocity vector are stored as a function of position in the computational domain. A point is then selected at a desired position in the flowfield, and a particle is moved along the local velocity vector at that point over a small time increment. When the particle arrives at a new position, it is again directed along the local velocity vector. This procedure is repeated stepwise in time until the particle exits the computational domain. Figure 16 clearly shows the particle movement from the computational domain through the fountain and wall jet. The figure demonstrates the capability of the graphics routine to rotate the flowfield, which can be done about each of the three axes, so that the pathlines are visible from any desired angle.

ONR has funded MDRL under a new contract N00014-79-C-0635 to extend the flowfield calculations of three-dimensional, turbulent impinging jets. Additional computations will be performed for equal-strength jets with normal impingement in addition to computations for the following cases: unequal-strength jets, normal impingement; equal-strength jets, inclined impingement; unequal-strength jets, inclined impingement; and an axisymmetric jet in crossflow. The accuracy of the computed flowfields for interacting jets with normal impingement and fountain formation will be determined in part through comparisons with data which will be obtained in an experimental program funded by ONR and conducted by the Aerodynamics Department of McDonnell Aircraft Company under contract N00014-79-C-0130.

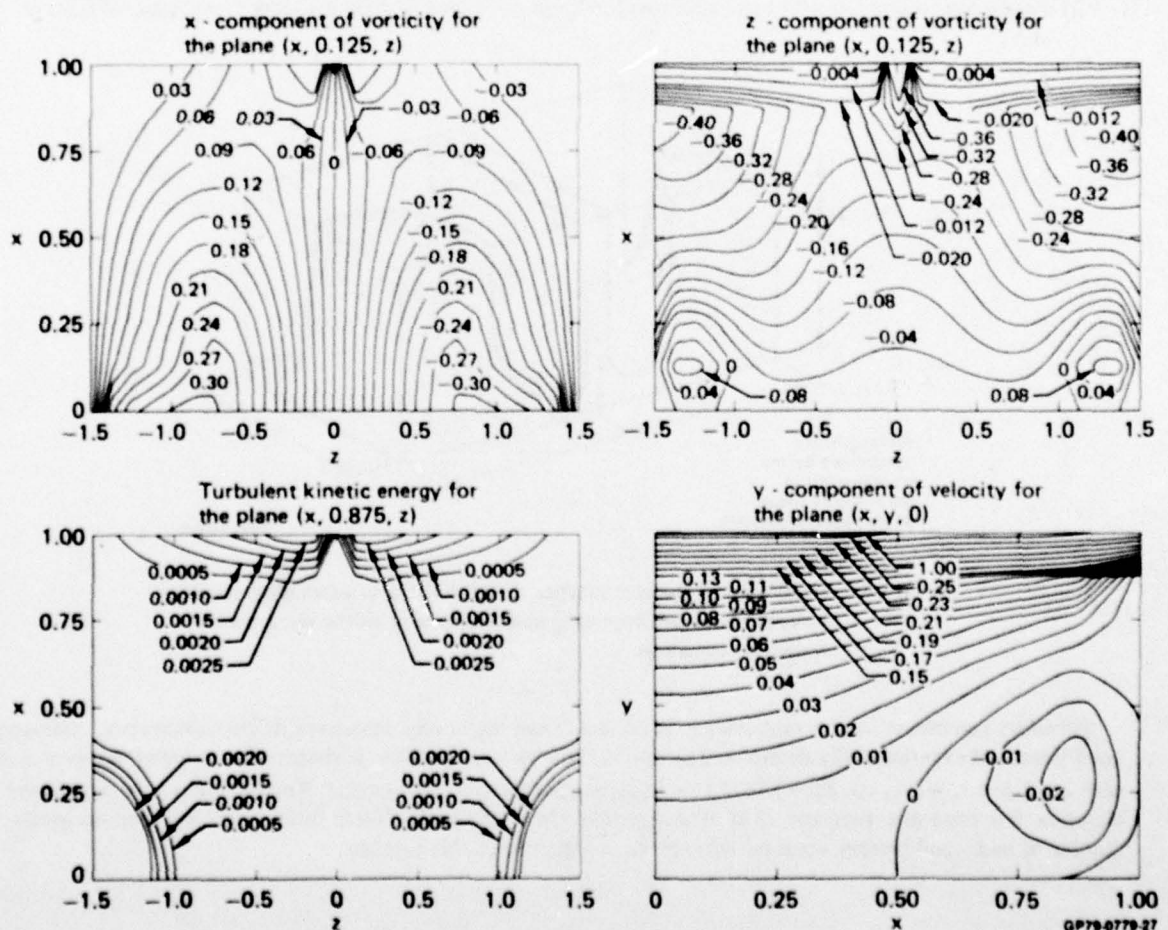
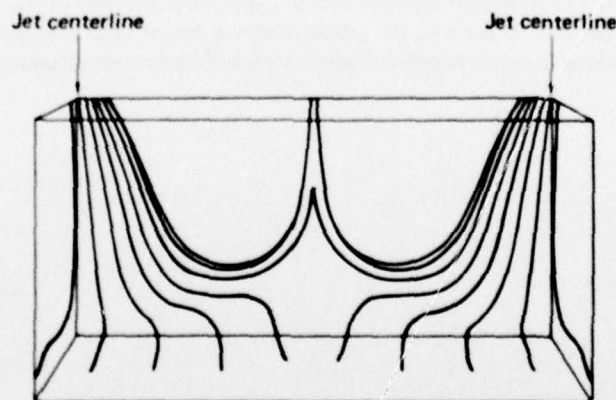
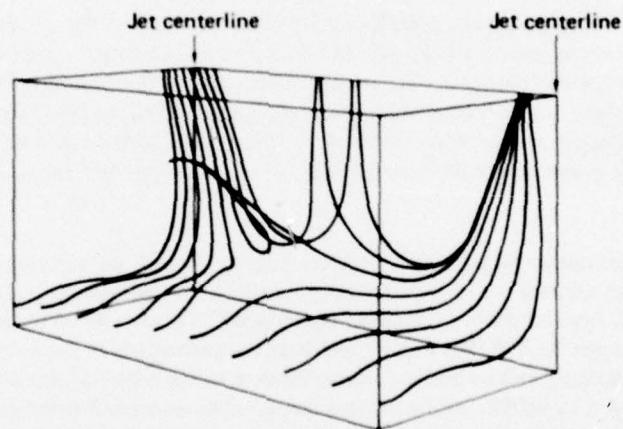
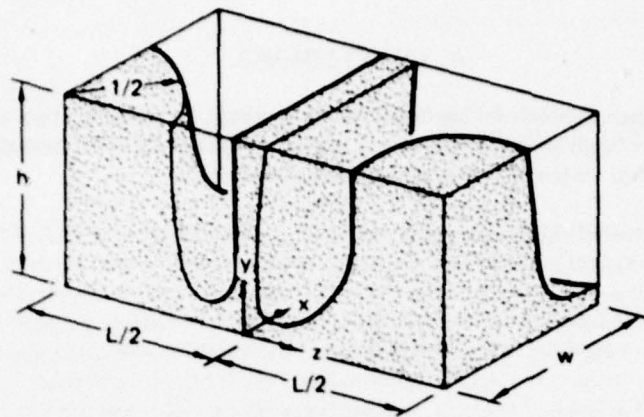


Figure 15. Representative contours for the incompressible, interacting jets in ground effect ($L = 3$, $h = 1$, $w = 1$, $Re = 1.00 \times 10^2$).



GP79-0779-26

Figure 16. Representative particle pathlines for the incompressible, interacting jets in ground effect ($L = 3$, $h = 1$, $w = 1$, $Re = 1.00 \times 10^2$).

4. CONCLUSIONS

McDonnell Douglas Research Laboratories has developed an approach for predicting two- and three-dimensional turbulent impinging jet flows based on a finite-difference solution of the fully elliptic, time-averaged conservation equations of fluid mechanics in conjunction with a turbulence model.

In the first year of a contracted research program with ONR, MDRL developed a method for the computation of planar, incompressible, turbulent lift jets in the proximity of airframe and ground surfaces. The equations are cast in terms of stream function and vorticity and are solved using an algorithm which provides convergent solutions for a wide range in Reynolds number. In the second year of the program, MDRL generalized the planar jet analysis to include the effects of compressibility. Comparisons between theory and experiment show reasonable agreement, although additional work is necessary to improve the turbulence modeling and a computer with storage capacity greater than the CYBER 175 is required to obtain accurate solutions for higher test Reynolds numbers. A basic conclusion drawn from the planar-jet studies is that contouring base area away from lift nozzle exits and perhaps the use of nozzle exit extensions will significantly reduce aircraft undersurface suck-down loads.

In the third year of the ONR contract work, MDRL developed a procedure for the calculation of three-dimensional, incompressible, turbulent lift jets in ground effect, with emphasis on a configuration comprised of two interacting jets with fountain formation. The equations are solved using a potential-function/vorticity formulation and an augmented, finite-difference algorithm to ensure convergence at high Reynolds numbers. The computed flowfield, displayed using a computer graphics routine that constructs particle pathlines, demonstrates the expected qualitative behavior. However, additional computations and comparisons with data are required to quantitatively evaluate the procedure.

Further work will be carried out by MDRL under ONR contract to improve the accuracy, efficiency, and generality of the present approach for solution of the Navier-Stokes equations for impinging jets. As Walters and Henderson² state in their report "V/STOL Aerodynamics Technology Assessment": "From a heuristic point of view, computerized analysis and prediction techniques for V/STOL aircraft performance, particularly in the hovering mode, must eventually take into account the viscosity and turbulence effects inherent in the Navier-Stokes equations." While the Navier-Stokes analysis developed by MDRL cannot provide the flowfield associated with a complete VTOL aircraft in ground effect, it can provide useful information on the jet entrainment and fountain flow required in potential flow paneling methods that are used to represent complete aircraft configurations. Data of this type cannot always be obtained precisely through experiment. Moreover, the solution scheme described in this paper can be applied to a variety of other problems of interest in subsonic aerodynamics, such as flow in internal passages.

REFERENCES

1. A. Rubel, *Computations of Jet Impingement on a Flat Surface*, AIAA Paper No. 78-207, 1978.
2. M. Walters and C. Henderson, *V/STOL Aerodynamics Technology Assessment*, Naval Air Development Center, Interim Report AIRTASK NO. A03V-320D/001 B/7F41-400-000, 15 May 1978.
3. A. Rubel, *Computational Techniques for the Calculation of Inviscid Rotational Jet Impingement*, AIAA Paper No. 78-1212, 1978.
4. M.W. Rubesin and W.C. Rose, *The Turbulent Mean-Flow, Reynolds-Stress, and Heat-Flux Equations in Mass-Averaged Dependent Variables*, NASA TM X-62, 248, March 1973.
5. A. Favre, *Equations des Gaz Turbulents Compressibles*, J. Méc. 4, 361 (1965).
6. D.R. Kotansky and W.W. Bower, *Viscous Flowfields and Airframe Forces Induced by Two-Dimensional Lift Jets in Ground Effect*, Office of Naval Research Report ONR-CR215-246-1, March 1977.
7. W.W. Bower, *Compressible Viscous Flowfields and Airframe Forces Induced by Two-Dimensional Lift Jets in Ground Effect*, Office of Naval Research Report ONR-CR215-246-2, March 1978.
8. M. Wolfshtein, *Convection Processes in Turbulent Impinging Jets*, Report SF/R/2, Department of Mechanical Engineering, Imperial College of Science and Technology, November 1967.
9. M.W. Rubesin, *A One-Equation Model of Turbulence for Use with the Compressible Navier-Stokes Equations*, NASA TM X-73, 128, April 1976.
10. W.P. Jones and B.E. Launder, *The Calculation of Low-Reynolds Number Phenomena with a Two-Equation Model of Turbulence*, Int. J. Heat Mass Transfer 16, 1119 (1973).
11. K.N. Ghia, W.L. Hankey, Jr., and J.K. Hodge, *Study of Incompressible Navier-Stokes Equations in Primitive Variables Using Implicit Numerical Technique*, Proceedings of the AIAA 3rd Computational Fluid Dynamics Conference, June 1977, pp. 156-167.
12. P.M. Worsøe-Schmidt and G. Leppert, *Heat Transfer and Friction for Laminar Flow of Gas in a Circular Tube at High Heating Rate*, Int. J. Heat Mass Transfer 8, 1281 (1965).
13. G.H. Hoffman, *Calculation of Separated Flows in Internal Passages*, Proceedings of a Workshop on Prediction Methods for Jet V/STOL Propulsion Aerodynamics 1, 114 (1975).
14. J.J. Schauer and R.H. Eustis, *The Flow Development and Heat Transfer Characteristics of Plane Turbulent Impinging Jets*, TR3, Department of Mechanical Engineering, Stanford University, September 1963.
15. R. Gardon and J.C. Akfirat, *The Role of Turbulence in Determining the Heat Transfer Characteristics of Impinging Jets*, Int. J. Heat Mass Transfer, 8, 1261 (1965).
16. D.R. Kotansky and W.W. Bower, *A Basic Study of the VTOL Ground Effect Problem for Planar Flow*, J. Aircraft 15, 214 (1978).
17. Y.A.S. Aregbesola and D.M. Burley, *The Vector and Scalar Potential Method for the Numerical Solution of Two- and Three-Dimensional Navier-Stokes Equations*, J. Comp. Phys. 24, 398 (1977).
18. G.J. Hirasaki and J.D. Hellums, *Boundary Conditions on the Vector and Scalar Potentials in Viscous Three-Dimensional Hydrodynamics*, Quart. Appl. Math. 28, 293 (1970).

APPENDIX:
DEFINITIONS OF FUNCTIONS APPEARING IN THE
GOVERNING EQUATIONS FOR PLANAR FLOW

$$\phi_1 = \frac{1}{\bar{\rho}^2} \frac{\partial \psi}{\partial x} \left(\frac{\partial \bar{\rho}}{\partial x} \frac{\partial^2 \psi}{\partial x \partial y} - \frac{\partial \bar{\rho}}{\partial y} \frac{\partial^2 \psi}{\partial x^2} \right) - \frac{1}{\bar{\rho}^2} \frac{\partial \psi}{\partial y} \left(\frac{\partial \bar{\rho}}{\partial y} \frac{\partial^2 \psi}{\partial x \partial y} - \frac{\partial \bar{\rho}}{\partial x} \frac{\partial^2 \psi}{\partial y^2} \right) \quad (\text{A-1})$$

$$\begin{aligned} \phi_2 = & \frac{1}{\bar{\rho}} \left(\frac{\partial^2 \bar{\mu}_{\text{eff}}}{\partial x^2} - \frac{\partial^2 \bar{\mu}_{\text{eff}}}{\partial x \partial y} \right) \left(\frac{\partial^2 \psi}{\partial y^2} - \frac{\partial^2 \psi}{\partial x^2} - \frac{1}{\bar{\rho}} \frac{\partial \bar{\rho}}{\partial y} \frac{\partial \psi}{\partial y} + \frac{1}{\bar{\rho}} \frac{\partial \bar{\rho}}{\partial x} \frac{\partial \psi}{\partial x} \right) + \frac{2}{\bar{\rho}} \frac{\partial^2 \bar{\mu}_{\text{eff}}}{\partial x \partial y} \\ & \left(\frac{1}{\bar{\rho}} \frac{\partial \bar{\rho}}{\partial y} \frac{\partial \psi}{\partial x} + \frac{1}{\bar{\rho}} \frac{\partial \bar{\rho}}{\partial x} \frac{\partial \psi}{\partial y} - 2 \frac{\partial^2 \psi}{\partial x \partial y} \right) + \frac{2}{\bar{\rho}^2} \frac{\partial \bar{\mu}_{\text{eff}}}{\partial x} \left\{ \left(\frac{2}{\bar{\rho}} \frac{\partial \bar{\rho}}{\partial x} \frac{\partial \bar{\rho}}{\partial y} - \frac{\partial^2 \bar{\rho}}{\partial x \partial y} \right) \frac{\partial \psi}{\partial y} + \frac{\partial \bar{\rho}}{\partial y} \frac{\partial^2 \psi}{\partial x \partial y} - \frac{\partial \bar{\rho}}{\partial x} \frac{\partial^2 \psi}{\partial y^2} \right. \\ & + \left. \left[\frac{\partial^2 \bar{\rho}}{\partial y^2} - \frac{2}{\bar{\rho}} \left(\frac{\partial \bar{\rho}}{\partial y} \right)^2 \right] \frac{\partial \psi}{\partial x} \right\} + \frac{2}{\bar{\rho}^2} \frac{\partial \bar{\mu}_{\text{eff}}}{\partial y} \left\{ \left(\frac{2}{\bar{\rho}} \frac{\partial \bar{\rho}}{\partial x} \frac{\partial \bar{\rho}}{\partial y} - \frac{\partial^2 \bar{\rho}}{\partial x \partial y} \right) \frac{\partial \psi}{\partial x} + \frac{\partial \bar{\rho}}{\partial x} \frac{\partial^2 \psi}{\partial x \partial y} - \frac{\partial \bar{\rho}}{\partial y} \frac{\partial^2 \psi}{\partial x^2} \right. \\ & + \left. \left[\frac{\partial^2 \bar{\rho}}{\partial x^2} - \frac{2}{\bar{\rho}} \left(\frac{\partial \bar{\rho}}{\partial x} \right)^2 \right] \frac{\partial \psi}{\partial y} \right\} \end{aligned} \quad (\text{A-2})$$

$$\phi_3 = \frac{2}{3} \left[\frac{3}{\bar{\rho}} \frac{\partial^2 \psi}{\partial x \partial y} - \frac{1}{\bar{\rho}^2} \left(2 \frac{\partial \bar{\rho}}{\partial x} \frac{\partial \psi}{\partial y} + \frac{\partial \bar{\rho}}{\partial y} \frac{\partial \psi}{\partial x} \right) \right] \quad (\text{A-3})$$

$$\begin{aligned} \phi_4 = & \frac{8}{3\bar{\rho}^2} \left[\frac{2}{\bar{\rho}} \left(\frac{\partial \bar{\rho}}{\partial x} \right)^2 + \frac{2}{\bar{\rho}} \left(\frac{\partial \bar{\rho}}{\partial y} \right)^2 - \frac{\partial^2 \bar{\rho}}{\partial x^2} - \frac{\partial^2 \bar{\rho}}{\partial y^2} \right] \frac{\partial \psi}{\partial y} + \frac{8}{3\bar{\rho}} \left(\frac{\partial^3 \psi}{\partial y^3} + \frac{\partial^3 \psi}{\partial x^2 \partial y} - \frac{2}{\bar{\rho}} \frac{\partial \bar{\rho}}{\partial x} \frac{\partial^2 \psi}{\partial x \partial y} \right. \\ & \left. - \frac{2}{\bar{\rho}} \frac{\partial \bar{\rho}}{\partial y} \frac{\partial^2 \psi}{\partial y^2} \right) + \frac{2}{3} \frac{\partial \omega}{\partial y} \end{aligned} \quad (\text{A-4})$$

$$\phi_5 = \frac{1}{\bar{\rho}} \left(\frac{\partial^2 \psi}{\partial y^2} - \frac{\partial^2 \psi}{\partial x^2} + \frac{1}{\bar{\rho}} \frac{\partial \bar{\rho}}{\partial x} \frac{\partial \psi}{\partial x} - \frac{1}{\bar{\rho}} \frac{\partial \bar{\rho}}{\partial y} \frac{\partial \psi}{\partial y} \right) \quad (\text{A-5})$$

$$\begin{aligned} \phi_6 = & \frac{8}{3\bar{\rho}^2} \left[-\frac{2}{\bar{\rho}} \left(\frac{\partial \bar{\rho}}{\partial x} \right)^2 - \frac{2}{\bar{\rho}} \left(\frac{\partial \bar{\rho}}{\partial y} \right)^2 + \frac{\partial^2 \bar{\rho}}{\partial x^2} + \frac{\partial^2 \bar{\rho}}{\partial y^2} \right] \frac{\partial \psi}{\partial x} + \frac{8}{3\bar{\rho}} \left(\frac{2}{\bar{\rho}} \frac{\partial \bar{\rho}}{\partial x} \frac{\partial^2 \psi}{\partial x^2} - \frac{\partial^3 \psi}{\partial x^3} + \frac{2}{\bar{\rho}} \frac{\partial \bar{\rho}}{\partial y} \frac{\partial^2 \psi}{\partial x \partial y} \right. \\ & \left. - \frac{\partial^3 \psi}{\partial x \partial y^2} \right) - \frac{2}{3} \frac{\partial \omega}{\partial x} \end{aligned} \quad (\text{A-6})$$

$$\phi_7 = \frac{2}{3} \left[-\frac{3}{\bar{\rho}} \frac{\partial^2 \psi}{\partial x \partial y} + \frac{1}{\bar{\rho}^2} \left(2 \frac{\partial \bar{\rho}}{\partial y} \frac{\partial \psi}{\partial x} + \frac{\partial \bar{\rho}}{\partial x} \frac{\partial \psi}{\partial y} \right) \right] \quad (\text{A-7})$$

$$\begin{aligned}
\phi_8 = & \left\{ \left[\frac{3}{\bar{\rho}} \left(\frac{\partial \bar{\rho}}{\partial x} \right)^2 - \frac{\partial^2 \bar{\rho}}{\partial x^2} + \frac{3}{\bar{\rho}} \left(\frac{\partial \bar{\rho}}{\partial y} \right)^2 - 3 \frac{\partial^2 \bar{\rho}}{\partial y^2} \right] \frac{2}{\bar{\rho}^3} \frac{\partial \bar{\rho}}{\partial y} + \left[\frac{\partial^3 \bar{\rho}}{\partial x^2 \partial y} \right. \right. \\
& + \left. \frac{\partial^3 \bar{\rho}}{\partial y^3} - \frac{4}{\bar{\rho}} \frac{\partial \bar{\rho}}{\partial x} \frac{\partial^2 \bar{\rho}}{\partial x \partial y} \right] \frac{1}{\bar{\rho}^2} \left. \right\} \frac{\partial \psi}{\partial x} + \left[\frac{\partial^2 \bar{\rho}}{\partial x \partial y} - \frac{2}{\bar{\rho}} \frac{\partial \bar{\rho}}{\partial x} \frac{\partial \bar{\rho}}{\partial y} \right] \frac{2}{\bar{\rho}^2} \left(\frac{\partial^2 \psi}{\partial x^2} - \frac{\partial^2 \psi}{\partial y^2} \right) \\
& - \left\{ \left[\frac{3}{\bar{\rho}} \left(\frac{\partial \bar{\rho}}{\partial x} \right)^2 - 3 \frac{\partial^2 \bar{\rho}}{\partial x^2} + \frac{3}{\bar{\rho}} \left(\frac{\partial \bar{\rho}}{\partial y} \right)^2 - \frac{\partial^2 \bar{\rho}}{\partial y^2} \right] \frac{2}{\bar{\rho}^3} \frac{\partial \bar{\rho}}{\partial x} - \left[\frac{\partial^3 \bar{\rho}}{\partial x \partial y^2} \right. \right. \\
& + \left. \frac{\partial^3 \bar{\rho}}{\partial x^3} - \frac{4}{\bar{\rho}} \frac{\partial \bar{\rho}}{\partial y} \frac{\partial^2 \bar{\rho}}{\partial x \partial y} \right] \frac{1}{\bar{\rho}^2} \left. \right\} \frac{\partial \psi}{\partial y} + \left\{ \frac{2}{\bar{\rho}} \left[\left(\frac{\partial \bar{\rho}}{\partial x} \right)^2 - \left(\frac{\partial \bar{\rho}}{\partial y} \right)^2 \right] - \frac{\partial^2 \bar{\rho}}{\partial x^2} \right. \\
& + \left. \frac{\partial^2 \bar{\rho}}{\partial y^2} \right\} \frac{2}{\bar{\rho}^2} \frac{\partial^2 \psi}{\partial x \partial y} + \frac{1}{\bar{\rho}^2} \frac{\partial \bar{\rho}}{\partial y} \left(\frac{\partial^3 \psi}{\partial x \partial y^2} + \frac{\partial^3 \psi}{\partial x^3} \right) - \frac{1}{\bar{\rho}^2} \frac{\partial \bar{\rho}}{\partial x} \left(\frac{\partial^3 \psi}{\partial x^2 \partial y} + \frac{\partial^3 \psi}{\partial y^3} \right) \quad (A-8)
\end{aligned}$$

$$\begin{aligned}
\phi_9 = & \frac{1}{\bar{\rho}^2} \left(\frac{\partial \psi}{\partial x} \right)^2 \left[\frac{2}{\bar{\rho}} \left(\frac{\partial \bar{\rho}}{\partial y} \right)^2 - \frac{\partial^2 \bar{\rho}}{\partial y^2} \right] + \frac{1}{\bar{\rho}^2} \left(\frac{\partial \psi}{\partial y} \right)^2 \left[\frac{2}{\bar{\rho}} \left(\frac{\partial \bar{\rho}}{\partial x} \right)^2 - \frac{\partial^2 \bar{\rho}}{\partial x^2} \right] \\
& + \frac{2}{\bar{\rho}} \frac{\partial^2 \psi}{\partial x \partial y} \left(\frac{\partial^2 \psi}{\partial x \partial y} - \frac{1}{\bar{\rho}} \frac{\partial \bar{\rho}}{\partial x} \frac{\partial \psi}{\partial y} - \frac{1}{\bar{\rho}} \frac{\partial \bar{\rho}}{\partial y} \frac{\partial \psi}{\partial x} \right) + \frac{2}{\bar{\rho}^2} \frac{\partial \psi}{\partial x} \frac{\partial \psi}{\partial y} \left(\frac{\partial^2 \bar{\rho}}{\partial x \partial y} - \frac{2}{\bar{\rho}} \frac{\partial \bar{\rho}}{\partial x} \frac{\partial \bar{\rho}}{\partial y} \right) \\
& + \frac{2}{\bar{\rho}} \left(\frac{1}{\bar{\rho}} \frac{\partial \bar{\rho}}{\partial x} \frac{\partial \psi}{\partial x} \frac{\partial^2 \psi}{\partial y^2} + \frac{1}{\bar{\rho}} \frac{\partial \bar{\rho}}{\partial y} \frac{\partial^2 \psi}{\partial x^2} \frac{\partial \psi}{\partial y} - \frac{\partial^2 \psi}{\partial x^2} \frac{\partial^2 \psi}{\partial y^2} \right) \quad (A-9)
\end{aligned}$$

$$\phi_{10} = \frac{1}{\bar{\rho}} \left[\left(\frac{\partial^2 \psi}{\partial x \partial y} + \frac{1}{\bar{\rho}} \frac{\partial \bar{\rho}}{\partial y} \frac{\partial \psi}{\partial x} - \frac{1}{\bar{\rho}} \frac{\partial \bar{\rho}}{\partial x} \frac{\partial \psi}{\partial y} \right) \frac{\partial \psi}{\partial y} - \frac{\partial \psi}{\partial x} \frac{\partial^2 \psi}{\partial y^2} \right] \quad (A-10)$$

$$\phi_{11} = \frac{1}{\bar{\rho}} \left[\left(\frac{\partial^2 \psi}{\partial x \partial y} + \frac{1}{\bar{\rho}} \frac{\partial \bar{\rho}}{\partial x} \frac{\partial \psi}{\partial y} - \frac{1}{\bar{\rho}} \frac{\partial \bar{\rho}}{\partial y} \frac{\partial \psi}{\partial x} \right) \frac{\partial \psi}{\partial x} - \frac{\partial^2 \psi}{\partial x^2} \frac{\partial \psi}{\partial y} \right] \quad (A-11)$$

$$\begin{aligned}
\phi_{12} = & \bar{\mu}_{\text{eff}} \left\{ \frac{4}{\bar{\rho}^2} \left(\frac{\partial^2 \psi}{\partial x \partial y} \right) \left[\frac{\partial^2 \psi}{\partial x \partial y} - \frac{1}{\bar{\rho}} \frac{\partial \bar{\rho}}{\partial y} \frac{\partial \psi}{\partial x} - \frac{1}{\bar{\rho}} \frac{\partial \bar{\rho}}{\partial x} \frac{\partial \psi}{\partial y} \right] \right. \\
& + \frac{4}{3} \frac{1}{\bar{\rho}^4} \left[\left(\frac{\partial \bar{\rho}}{\partial y} \right)^2 \left(\frac{\partial \psi}{\partial x} \right)^2 + \left(\frac{\partial \bar{\rho}}{\partial x} \right)^2 \left(\frac{\partial \psi}{\partial y} \right)^2 + \frac{\partial \bar{\rho}}{\partial x} \frac{\partial \bar{\rho}}{\partial y} \frac{\partial \psi}{\partial x} \frac{\partial \psi}{\partial y} \right] \\
& + \left. \frac{1}{\bar{\rho}^4} \left(\frac{\partial \bar{\rho}}{\partial x} \frac{\partial \psi}{\partial x} - \frac{\partial \bar{\rho}}{\partial y} \frac{\partial \psi}{\partial y} \right)^2 + \frac{2}{\bar{\rho}^3} \left(\frac{\partial \bar{\rho}}{\partial x} \frac{\partial \psi}{\partial x} - \frac{\partial \bar{\rho}}{\partial y} \frac{\partial \psi}{\partial y} \right) \left(\frac{\partial^2 \psi}{\partial y^2} - \frac{\partial^2 \psi}{\partial x^2} \right) + \frac{1}{\bar{\rho}^2} \left(\frac{\partial^2 \psi}{\partial x^2} - \frac{\partial^2 \psi}{\partial y^2} \right)^2 \right\} \quad (A-12)
\end{aligned}$$

$$\begin{aligned}
\phi_{13} = \bar{\mu}_{\text{turb}} \Bigg\{ & \frac{4}{\bar{\rho}^2} \left(\frac{\partial^2 \psi}{\partial x \partial y} \right) \left[\frac{\partial^2 \psi}{\partial x \partial y} - \frac{1}{\bar{\rho}} \frac{\partial \bar{\rho}}{\partial y} \frac{\partial \psi}{\partial x} - \frac{1}{\bar{\rho}} \frac{\partial \bar{\rho}}{\partial x} \frac{\partial \psi}{\partial y} \right] \\
& + \frac{4}{3} \frac{1}{\bar{\rho}^4} \left[\left(\frac{\partial \bar{\rho}}{\partial y} \right)^2 \left(\frac{\partial \psi}{\partial x} \right)^2 + \left(\frac{\partial \bar{\rho}}{\partial x} \right)^2 \left(\frac{\partial \psi}{\partial y} \right)^2 + \frac{\partial \bar{\rho}}{\partial x} \frac{\partial \bar{\rho}}{\partial y} \frac{\partial \psi}{\partial x} \frac{\partial \psi}{\partial y} \right] \\
& + \frac{1}{\bar{\rho}^4} \left(\frac{\partial \bar{\rho}}{\partial x} \frac{\partial \psi}{\partial x} - \frac{\partial \bar{\rho}}{\partial y} \frac{\partial \psi}{\partial y} \right)^2 + \frac{2}{\bar{\rho}^3} \left(\frac{\partial \bar{\rho}}{\partial x} \frac{\partial \psi}{\partial x} - \frac{\partial \bar{\rho}}{\partial y} \frac{\partial \psi}{\partial y} \right) \left(\frac{\partial^2 \psi}{\partial y^2} - \frac{\partial^2 \psi}{\partial x^2} \right) + \frac{1}{\bar{\rho}^2} \left(\frac{\partial^2 \psi}{\partial x^2} - \frac{\partial^2 \psi}{\partial y^2} \right)^2 \Bigg\} \quad (\text{A-13})
\end{aligned}$$

DISTRIBUTION LIST

Office of Naval Research		U.S. Naval Postgraduate School	
800 N. Quincy St.		Monterey, CA 93940	
Arlington, VA 22217		Dept. of Aeronautics (Code 57)	1
ONR 211	4	Library	1
ONR 430B	1		
Office of Naval Research Branch		Superintendent	
Office		U.S. Naval Academy	
1030 E. Green St.		Annapolis, MD 21402	1
Pasadena, CA 91106	1		
Office of Naval Research Branch		NASA Ames Research Center	
Office		Moffett Field, CA 94035	
Bldg. 114 Section D		FAE Branch (Dr. T. Gregory)	1
666 Summer St.			
Boston, MA 02210	1	NASA Langley Research Center	
		Hampton, VA 23665	
		Mr. R. Margason	1
Office of Naval Research Branch		Wright Patterson Air Force Base	
Office		Dayton, OH 45433	
536 South Clark St.		Aero & Airframe Branch (Dr. T. Weeks)	1
Chicago, IL 60605	1		
Naval Research Laboratory		Air Force Office of Scientific Research	
Washington, DC 20375		Bolling AFB, DC 20332	
Code 2627	1	Code NA (Dr. J. Wilson)	1
Code 2629	1		
Defense Documentation Center		Defense Advanced Research Projects	
Bldg. 5 Cameron Station		Agency	
Alexandria, VA 22314	12	1400 Wilson Boulevard	
		Arlington, VA 22209	
		Mr. R. Moore	1
Naval Air Systems Command		Lockheed Missiles & Space Co., Inc.	
Washington, DC 20361		Huntsville Research & Engineering	
AIR 320D (Mr. R. Siewert)	1	Center	
AIR 5301-33B (Mr. Lynn Trobaugh)	1	P.O. Box 1103	
AIR 03PA (H. Andrews)	1	Huntsville, AL 35807	
AIR ADPO-16 (CDR J. Farley)	1	Mr. A. Zalay	1
Naval Air Development Center		Nielsen Engineering & Research, Inc.	
Warminster, PA 18974		510 Clyde Avenue	
Code 6053 (Mr. C. Mazza)	2	Mountain View, CA 94043	1
David Taylor Naval Ship Research and		McDonnell Aircraft Company	
Development Center		P.O. Box 516	
Bethesda, MD 20084		St. Louis, MO 63166	
Code 16 (Dr. H. Chaplin)	1	Aerodynamics (Dr. D. Kotansky)	1
Code 1660 (Mr. J. Nichols)	1	Propulsion (Mr. J. Kamman)	1
Code 1613 (Mr. R. Schaeffer)	1		
Code 1843 (Ms. J. Schot)	1		
Code 522.3 Aero Library	1		

Vought Corporation
Advanced Technology Center, Inc.
P.O. Box 6144
Dallas, TX 75222
Dr. C.S. Wells, Jr.

1

Grumman Aerospace Corporation
Bethpage, NY 11714
Research Dept. (Dr. R. Melnik)
Advanced Dev. Dept. (Mr. F. Berger)

1

1

Rockwell International
Columbus Aircraft Division
Columbus, OH 43216
Research Dept. (Dr. P. Bevilacqua)

1

University of Southern California
Dept. of Aerospace Engineering
University Park
Los Angeles, CA 90007
Prof. John Laufer

1

Flow Research Inc.
P.O. Box 5040
Kent, WA 98031
Dr. E. Murman

1

Virginia Polytechnic Institute
Dept. of Engr. Sciences & Mechanics
Blacksburg, VA 24061

1

University of Maryland
Dept. of Aerospace Engr.
College Park, MD 20742
Dr. J. D. Anderson, Jr.

1

United Aircraft Corporation
Research Laboratories
Silver Lane
East Hartford, CT 06108
Dr. M. Werle

1

Polytechnic Institute of New York
Long Island Center
Dept. of Aero Engr. and Applied
Mechanics
Route 110
Farmingdale, NY 11735

1

Scientific Research Associates, Inc.
P.O. Box 498
Glastonbury, CT 06033
Dr. H. McDonald

1

Douglas Aircraft Company
3855 Lakewood Blvd.
Long Beach, CA 90808
Dr. T. Cebeci

1

National Science Foundation
Engineering Division
1800 G St., NW
Washington, DC 20550

1

General Dynamics/Fort Worth Division
Aerospace Tech. Dept.
Fort Worth, TX 76101
Dr. W. Foley

1

University of Michigan
Dept. of Aerospace Engineering
Ann Arbor, MI 48104
Prof. T.C. Adamson, Jr.

Ohio State University
Dept. of Aeronautical and
Astronautical Engineering
Columbus, OH 43210
Prof. Gerald M. Gregorek